Energy-efficient W-doped VO_2-based smart glasses by glancing angle co-deposition and subsequent rapid thermal annealing

A.J. Santos[a,b,c,*], A. Casas-Acuña[a,b], N. Martin[c], J.J. Jiménez[a,b], A. Krystianiak[d], O. Heintz[d], R. García[a,b], F.M. Morales[a,b]

[a] *IMEYMAT: Institute of Research on Electron Microscopy and Materials of the University of Cádiz, E-11510, Puerto Real, Spain.*

[b] *Department of Materials Science and Metallurgic Engineering, and Inorganic Chemistry, Faculty of Sciences, University of Cádiz, E-11510 Puerto Real, Spain.*

[c] *SUPMICROTECH, CNRS, Institut FEMTO-ST, 25000 Besançon Cedex, France.*

[d] *Laboratoire ICB, UMR 6303 CNRS, Univ. Bourgogne Franche-Comté, 9, Avenue Alain Savary, BP 47 870, 21078 Dijon Cedex, France.*

* Corresponding author: antonio.santos@uca.es

Abstract: This work reports on an original approach to the fabrication of 25 and 50 nm thick W-doped VO_2-based coatings which comprises the initial co-deposition, at glancing angles and in the presence of reactive oxygen, of alternating $VO_y/V_{0.85}W_{0.15}O_y$ multilayers with average W/V ratios between 1/99 and 5/95, and their subsequent rapid thermal annealing in air atmosphere. Exhaustive micro- and nanostructural, compositional, and optical characterizations of samples treated at reaction temperatures of 475 and 550 °C for times below 30 s confirmed the synthesis of homogeneous $V_xW_{1-x}O_2$-based films with unique thermochromic features strongly dependent on the dopant amounts. In general, a gradual lowering of the critical temperature to 37 °C during heating was achieved for the maximum doping of $x = 0.95$, albeit at the expense of some detriments in optical performances. The best and most balanced results were accomplished in a 50 nm layer doped at $x = 0.97$ (i.e. ~1 at% W) subjected to flash annealing at 550ºC, presenting a remarkable balance of light transmittance (52.0%), solar modulation capability (5.2%) and critical temperature drop (44ºC), which leads to a temperature drop rate of about 24 ºC per at% W. In addition, the hysteresis width and smoothness achieved make this coating potentially suitable for application in glazing exposed to direct solar radiation. The proposed methodologies, involving green-like reactions and single-layer designs, postulate as an attractive, plausible and cost-effective alternative for large-scale manufacturing of VO_2(M)-based smart coatings.

Keywords: Vanadium dioxide, W-doping, glancing angle co-deposition, rapid thermal annealing, Vis-NIR spectrophotometry, thermochromism, smart glazing

1. Introduction

In recent times, there has been a growing concern to minimize heat losses that occur through the windows of buildings and vehicles. Furthermore, the increasing use of large glazed surfaces to provide rooms with a greater amount of natural light amplifies the above energy transfer problem, which inevitably leads to a marked rise in total energy consumption and associated costs to guarantee satisfactory indoor thermal comfort[1,2]. In this light, passive thermochromic smart surfaces seem to be the most reasonable alternative to this energy inefficiency issue, as they can respond independently of external environmental conditions (such as light or heat) without the need of external electrical power (i.e., zero energy consumption) and/or user intervention[3–6].

Among thermochromic materials, vanadium dioxide (VO_2) stands out as one of the most promising for the next generation of smart windows[7–11]. It undergoes a thermally induced reversible metal-to-insulator transition (MIT) at relatively near room temperature (~68°C), which leads to dramatic changes in its optical properties in the near-infrared (NIR) range, from a low-temperature transparent monoclinic (M1) phase to a heat-blocking rutile (R) phase at high temperature[12–14]. However, the large-scale transfer of this technology has been mainly restricted due to obstacles related to VO_2 performance and production: (i) the need to reduce the MIT critical temperature (T_c) to environments comfortable for human beings while satisfying minimum requirements of solar modulation efficiency ($\Delta T_{sol} > 10\%$) and luminous transmittance ($T_{lum} > 60$)[15,16]; (ii) the great complexity, low efficiency and high cost of the main fabrication strategies, which stem from the difficulties encountered in the synthesis of the M1-VO_2 phase (large number of vanadium oxidation states, existence of different polymorphs for the same oxide)[17–20] as well as in its long-term stabilization[21,22].

Research has shown that doping VO_2 with high valence elements, such as W^{6+}[21,23–27], Nb^{5+}[28,29] or Mo^{6+}[30,31], is the most effective alternative for reducing T_c. In this sense, tungsten is the most widely used dopant, allowing drastic reduction rates of up to 20–28°C per at%[32]. However, even in small quantities, elemental doping becomes a real challenge as the introduction of heterogeneities often leads to some detrimental effects in T_{lum} and ΔT_{sol}[33]. The incorporation of dopants has also revealed to have a significant effect on other MIT-related features such as hysteresis width (W_H) and smoothness (S_H), both of relevance in the design and performance of smart windows. Notwithstanding, despite the numerous reports related to VO_2 doping found in the literature, these parameters have not been studied systematically and in depth to date.

Likewise, the characteristics of the MIT strongly depend on the fabrication processes of VO_2-based coatings. In general, thermal oxidation of V-W precursor films is the most widespread approach for achieving W-doped VO_2 coatings. Nevertheless, these methodologies often involve the establishment of highly controlled oxidative atmospheres or high vacuums, and further annealing with times longer than 15 min for temperatures between 450–500°C[24–26], which compromises their scalability in terms of associated glass damage. In this way, several authors have recently started to adopt more scalable strategies involving rapid thermal annealing (RTA) of VO_x-based precursor films in air atmosphere[34–36]. This approach offers the additional benefit of limiting the diffusion of sodium ions from the glass substrates into the VO_2 film during the post-deposition annealing process, thus avoiding a deterioration of the thermochromic properties of the coating[27]. However, most of these works lack precise control of the fundamental reaction parameters (i.e., heating and cooling rates and/or reaction temperature and times). Within this framework, our previous studies have revealed that, thanks to the fine control of deposition and annealing parameters, the fabrication of VO_2-based films on glass substrates can be achieved through simple two-step approaches consisting of RTA in air of porous V or VO_x films achieved through the GLancing Angle Deposition (GLAD) technique[37–39]. This enabled the fabrication of highly-efficient VO_2-based thermochromic coatings with remarkable decreases of the MIT temperature down to 53°C without elemental doping. Even so, phase transition temperatures thereby attained are insufficient for real application in smart glazing.

On the basis of our previous studies, and with the aim of further improving such manufacturing strategies, this work reports an original route to attain W-doped VO_2-based coatings on glass substrates by combining the co-deposition of $VO_y/V_{0.85}W_{0.15}O_y$ multilayers with zigzag GLAD arrangements and subsequent highly-controlled atmospheric rapid annealing. Comprehensive micro- and nanoscale structural and compositional characterizations of the fabricated films were addressed by X-ray photoelectron spectroscopy (XPS), scanning electron microscopy (SEM), grazing incidence X-ray diffraction (GIXRD), and scanning-transmission electron microscopy ((S)TEM) imaging techniques and spectroscopies. The optical thermochromic response of such surfaces was evaluated by variable temperature Vis-NIR spectrophotometry, placing special emphasis on the effects that the disposition and concentration of tungsten as well as the applied thermal annealing have on the key optical parameters for smart glazing applications (i.e., T_{lum}, ΔT_{sol}, T_c, W_H, S_H).

2. Materials and Methods

2.1. Deposition process

Thin films were deposited at room temperature by direct current (DC) magnetron sputtering using two opposite metallic targets (51 mm of diameter and 99.9% purity):

vanadium and tungsten. They were located inside a 40 L homemade vacuum chamber evacuated down to 10^{-5} Pa before each run by means of a turbomolecular pump backed by a primary pump. The distance between V and W target centers and the glass substrate (Menzel Gläser ® microscope slides) are fixed to 65 mm and 95 mm, respectively. On the basis of our previous studies[39], porous films with large surface-to-volume ratios and enhanced reactivity with oxygen were deposited by combining GLAD and Reactive Gas Pulsing Process (RGPP) techniques. The deposition angles α (average angle of incoming particle flux) relative to the substrate normal were set at α = 85º and 75º for vanadium and tungsten, respectively, with no rotation of the substrate (i.e., $\phi = 0$ rev h^{-1}). Argon was injected at a mass flow rate of 2.40 sccm and the pumping speed was maintained at $S = 13.5$ L s^{-1}, whereas the oxygen gas was periodically supplied into the sputtering chamber. A rectangular pulsed signal was employed for the oxygen flow rate with respect to time evolution. The pulsing period was set at $P = 16$ s. The maximum oxygen flow rate was $q_{O2Max} = 0.40$ sccm. It corresponds to the critical flow required to trigger the process in the compound sputtering mode. The minimum oxygen flow rate was $q_{O2min} = 0$ sccm, while the oxygen injection time (t_{ON}) was set at 8 s. Under this premise, $V_xW_{1-x}O_y$ films of different thicknesses, compositions and architectures were achieved by adjusting the deposition times of each element for fixed vanadium and tungsten target currents of 200 and 20 mA (minimum current to generate a stable W plasma), respectively. A schematic overview of the sputtering configuration is shown in **Figure 1**. Finally, samples were subjected to an azimuthal rotation of $\Phi = 180°$ at half the time required to achieve any given layer thickness to promote the fabrication of zigzag GLAD films of uniform overall layer thickness.

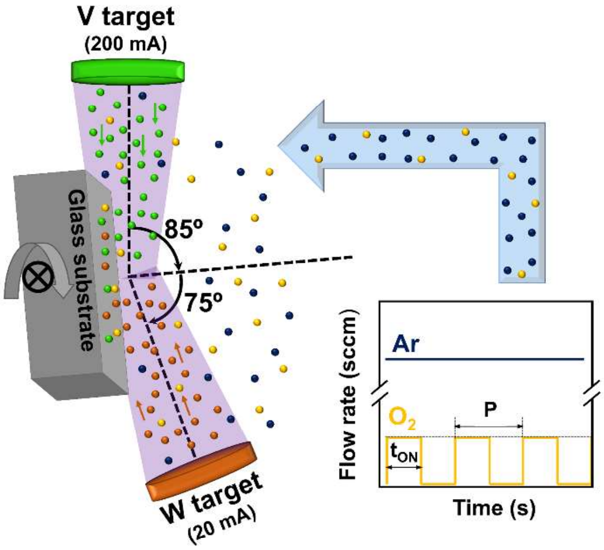

Figure 1. Schematic overview of the sputtering system used for the co-deposition of vanadium and tungsten oxide films combining GLAD and RGPP techniques.

2.2. Thermal treatments

After deposition, samples were thermally treated in a homemade reaction system. It consists in an Al_2O_3 tube in a furnace with SiC resistors able to reach temperatures of up to 1500°C, with an attached concentric steel tube and a high temperature steel-covered K-type thermocouple inside. This thermometer bar acts as an axle for a system of horizontal translation. At the end of the metallic tube nearby the furnace, the thermocouple crosses and fixes to a cylinder placed inside this tube, mechanized with a hitch to hang a combustion boat. Thus, the thermometer tip is always placed some millimeters over the center of this boat, which is an alumina crucible, allowing the temperature in the reaction zone to be monitored. The other end side also crosses and is fixed to another piece that is part of a handlebar used to slide the specimen holders inside and outside the furnace. In this way, by fixing a temperature in the center of the furnace, one is able to control the temperature increase (heating rate) by moving the boat more and more inside the furnace (for a more detailed overview of the reaction system, refer to previous studies[40]). Consequently, translation routines were prepared for reaching an average heating rate of 42ºC s^{-1}, as well as for adjusting longer or shorter reaction times at a desired temperature. Lastly, all samples were left to be cooled down in air to room temperature.

2.3. Structural, compositional and functional characterizations

X-ray photoelectron spectroscopy (XPS) data were acquired in a PHI VersaProbe 1 system using an Al Kα X-ray source (hυ = 1486.7 eV, power of 50 W) and a spot diameter of 200 micrometers. CasaXPS software was used for data treatment[41]. Topographic micrographs of oxidized samples were acquired using a Thermo Scientific Scios 2 DualBeam analytical focused ion beam scanning electron microscopy (FIB-SEM) system operating at 5 kV. This same facility was also used to prepare electron-transparent cross-section lamellae for (S)TEM analyses. High-resolution transmission electron microscopy (HRTEM) and high-angle annular dark-field imaging (HAADF) studies were carried out in a Thermo Scientific TALOS F200X analytical microscope working at an accelerating voltage of 200 kV. A Gatan Imaging Filter (GIF) Continuum system fitted in the Talos microscope was used for spatially-resolved electron energy-loss spectroscopy (EELS) analysis in scanning-transmission (STEM) mode. STEM-EELS 2D spectrum image (SI) data were acquired using a 2.5 mm diameter aperture and 0.05 eV/channel energy dispersion. The camera length was 47 mm, so the convergence and collection semi-angles were thus set to 10.5 and 20.0 mrad, respectively, and the probe current was about 150–175 pA depending on the experiment. In order to allow accurate chemical shift measurements, the Dual EELS mode was used to record nearly simultaneously both low-loss signal and the V-$L_{2,3}$ and O-K high-loss edges, at each pixel position. Dwell time of about 0.2 second per pixel was set to optimize the signal-to-noise ratio. The energy-dispersive X-ray spectroscopy (EDX) studies were carried out in this same microscope using a Super-X detection system that is constituted by four silicon drift detectors distributed around the sample to be analyzed. GIXRD scans were performed on a Malvern Panalytical Aeris diffractometer (Cu radiation) working at 30 kV (10 mA) and setting a grazing incidence angle of 0.8°. The thermochromic optical features of the fabricated W-doped VO_2 films were determined via transmission spectroscopy using a PerkinElmer Lambda 900 UV/VIS/NIR Spectrometer equipped with a THMS600 Linkam stage for temperature control. Vis-NIR transmittance spectra were recorded in the wavelength range of 350–2500 nm at selected temperatures in the range of 15–90ºC. For the dynamic monitoring of the thermally induced phase transition, the thermal evolution of the optical transmittance at a selected NIR wavelength (2000 nm) was recorded during consecutive heating-cooling cycles at a controlled rate of 1°C min^{-1}.

3. Results and discussion

3.1. Achieving VO_2-based coatings homogeneously doped with W

Preliminarily, it was necessary to adjust the co-deposition conditions to attain certain preferred doping ratios. For this purpose, three $V_xW_{1-x}O_y$ reference samples of 100 nm nominal thickness were deposited under the continuous conditions of target currents set out in the previous section (note that, at this stage, zigzag deposition was omitted to simplify/streamline fabrication processes). Given that, after thermal treatments, the W/V ratios of the $V_xW_{1-x}O_y$ precursors are preserved in the formed $V_xW_{1-x}O_2$, samples with $(1-x)/x$ ratios will be named as $(1-x)$W, for example, W/V=3/97 is denoted as 3W. XPS analyses of this group of 3 samples (see Section I of the Supplementary Material) revealed 15W compositions. However, it is well reported that the W/V ratios where tungsten works well as a dopant element in VO_2(M)-based smart glasses are typically between 1/99 and 5/95[21,23–27].

To overcome this limitation, a complementary strategy based on the deposition of alternating $VO_y/V_{0.85}W_{0.15}O_y$ multilayers was adopted to meet the desired dopant concentrations under the assumption that tungsten would diffuse and integrate into the VO_2(M) crystal structure homogeneously after subsequent thermal annealing. For this purpose, dopant deposition times were successfully calculated and controlled by opening and closing the W target shutter, allowing concentrations below that of 15W. When fabricating such nanostructures, the following rules were imposed with the aim of reproducibility: (i) minimum tungsten deposition time in each individual layer were not less than 5 s to avoid shutter-movement promoted artifacts; (ii) when conditions allowed it, a maximum number of up to 12 equidistant sublayers of $V_{0.85}W_{0.15}O_y$ were deposited in order to favor a further random and shorter diffusion of the dopant element. As an example, **Figure 2** shows the (S)TEM-EDX studies carried out on a 50 nm nominal thickness specimen consisting of 8 layers of $V_{0.85}W_{0.15}O_y$ intended to lead to an overall composition of $V_{0.95}W_{0.05}O_y$. It should be noted here that a lower number of sublayers than those conceptualized was intentionally deposited so as to make them individually thicker and thus more easily displayable by analytical (S)TEM. This also justifies the choice of the highest doping level for this example. Elemental maps of V and W (**Fig. 2(a–c)**) as well as EDX spectra acquired in W-rich and W-depleted regions (**Fig. 2(d)** and **(e)**) bring the fabricated multilayer nanostructures to light.

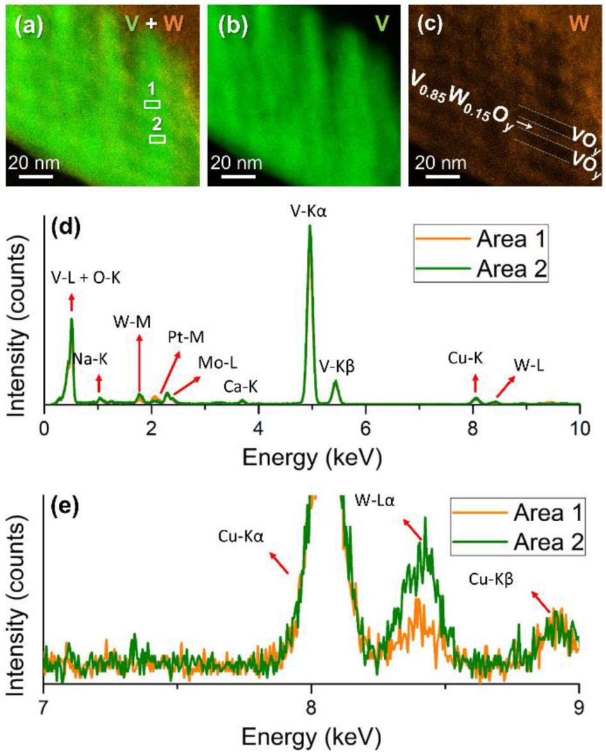

Figure 2. Transmission electron microscopy analyses performed on a nominally 50 nm-thick $VO_y/V_{0.85}W_{0.15}O_y$ multilayer film, for a target average tungsten concentration of 5W. (a–c) STEM-EDX net intensity maps obtained for V and W atoms. (d–e) EDX integrated spectra for the regions defined by the white squares in (a).

Once the optimal co-deposition conditions were established, zigzag multilayers of $VO_y/V_{0.85}W_{0.15}O_y$ with a nominal thickness of 25 and 50 nm (they allow best balance between transparency and heat blockage) and overall compositions to reach samples 1W, 2W, 3W and 5W were fabricated. Each of these samples was then subjected to two different optimal RTAs. Note that selected thicknesses and annealing conditions are based on the results obtained in our previous studies[39]. All the samples addressed in this study, together with their deposition and annealing conditions, are listed in **Table 1**.

Table 1. Deposition and thermal annealing conditions for the samples addressed in this study. τ_N is the nominal layer thickness, T_r is the reaction temperature, t_r is the reaction time.

Sample	**W doping (at%) in $V_xW_{1-x}O_2$**	**τ_N (nm)**	**Number of $V_{0.85}W_{0.15}O_y$ multilayers**	**T_r (°C)**	**t_r (s)**
1W_T50_475_30	0.33	50	8	475	30
1W_T50_550_1				550	1
1W_T25_475_10		25	4	475	10
1W_T25_500_1				500	1
2W_T50_475_30	0.67	50	12	475	30
2W_T50_550_1				550	1
2W_T25_475_10		25	6	475	10
2W_T25_500_1				500	1
3W_T50_475_30	1.00	50	12	475	30
3W_T50_550_1				550	1
3W_T37.5_525_1		37.5	9	525	1
3W_T25_475_10		25	6	475	10
3W_T25_500_1				500	1
5W_T50_475_30	1.67	50	12	475	30

3.2. Morphological, structural and compositional characterization

Figure 3 displays the top-view SEM micrographs acquired for 50 nm-thick 2W, 3W and 5W samples subjected to different RTAs at 475ºC or 550ºC. In this sense, two aspects need to be clarified: (i) only 50 nm samples were studied since they allow a better observation of the resulting morphologies (the 25 nm samples gave rise to hardly comparable microstructures formed by finer grains); (ii) the oxidation of the 5W sample was only successful at 475ºC and 30 s, i.e., at such dopant concentration, vanadium dioxide could not be synthesized by flash annealing at 550°C. The latter would be due to the fact that excessive doping can induce changes in the VO_2(M) reaction kinetics or favor the formation of other compounds. As can be observed in **Fig. 3 (a)** and **(b)**, for the same thermal annealing, increasing the dopant amount up to 3W results in the synthesis of a relatively homogeneous granular structure characterized by increasingly larger and equiaxed grains, which is characteristic of VO_2(M)[42,43]. On the contrary, the increase in reaction time, although at lower temperatures and for higher dopant concentrations, leads to the formation of more heterogeneous structures in which, in addition to grains similar to those of sample 3W_T50_550_1, other more elongated structures are observed which could be associated either with the formation of V_2O_5[44,45] or with solid solutions of V, W and O different from $V_xW_{1-x}O_2$[46]. This suggests that the formation of such compounds would be more favored when W is present in significant amounts.

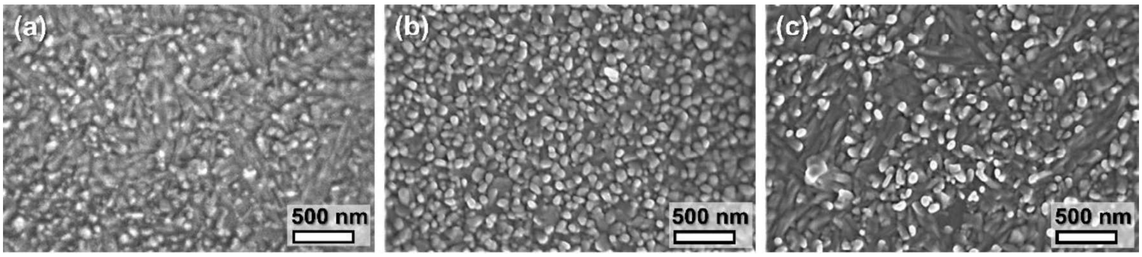

Figure 3. SEM micrographs depicting the surface morphology of samples (a) 2W_T50_550_1, (b) 3W_T50_550_1, and (c) 5W_T50_475_30.

Figure 4 shows the evolution of the crystalline structure of doped VO_2(M)-based samples 1W, 2W, and 3W subjected to the same instantaneous annealing at 550ºC. For comparative purposes, a representative undoped VO_2(M) sample was taken from previous studies. Three main features can be noticed here. On the one hand, it is observed that the inclusion of W favors, in some way, the formation of V_2O_5 (**Fig. 4(a)**). However, there is no clear relationship between the increase in the amounts of this compound and the proportion of dopant. Instead, what is undoubtedly evident is a progressive deterioration of the crystalline quality of the coating as the doping increases, becoming more apparent for the VO_2(M) diffracted signals (note that all diffractograms were collected under the same experimental conditions). It also translates into a progressive shift of the VO_2(M) (011) diffraction peaks towards lower 2θ angles, as can be seen in **Fig. 4(b)**. This trend, which has been widely reported in the literature[47–49], is typical of the $V_xW_{1-x}O_2$ system, which therefore confirms the effective doping of vanadium dioxide accompanied by a dilatation of the unit cell.

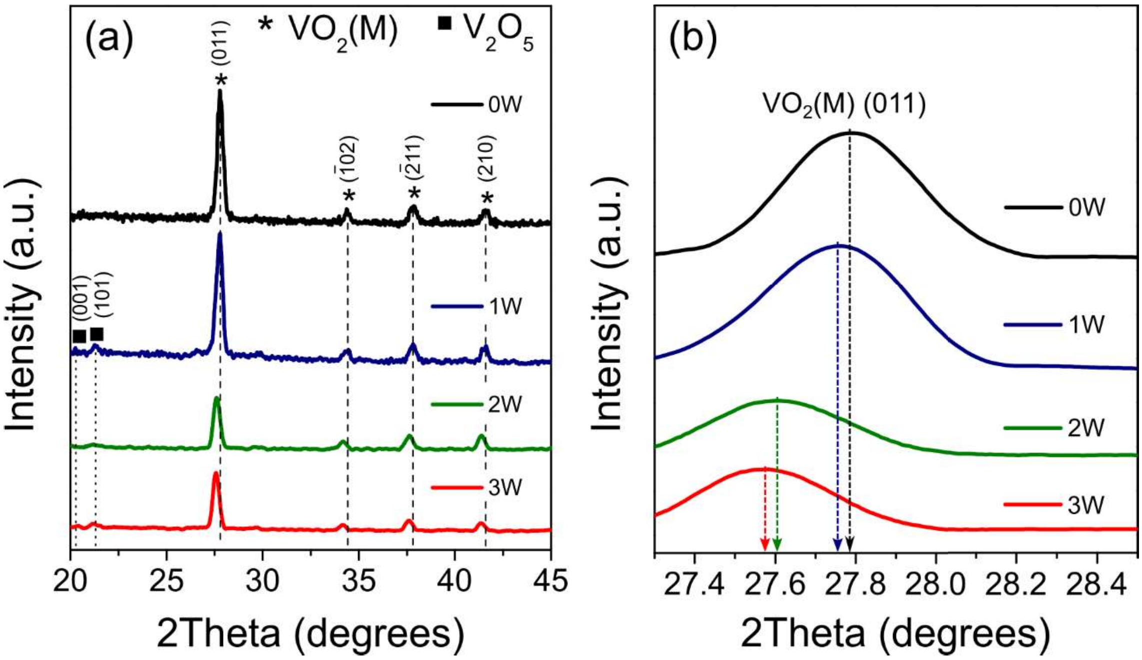

Figure 4. GIXRD scans for undoped and doped (1W, 2W and 3W) 50 nm-thick samples fabricated by flash annealing at 550°C. (b) Magnified view of the GIXRD diffractograms in the 2θ range of 27.3–28.5º. XRD patterns are indexed to the monoclinic VO_2 phase (JCPDS Card No. 82-0661 with space group P21/m) and V_2O_5 (JCPDS Card No. 89-0612).

For a deeper insight into the nanostructure and composition of the synthesized coatings, (S)TEM analyses were carried out for FIB lamellae of the same regions scanned by SEM (**Figure 5**). High-angle annular dark field (STEM-HAADF) and bright field (BF-TEM) micrographs allow to clearly identify two different layers within these films: A superficial one, relatively continuous and of amorphous nature (VO_y(II)), and a more internal one formed by crystalline grains (VO_y(I)). Furthermore, it seems that VO_y(II) overlayers become thicker for higher dopant concentrations. STEM-EELS spectra (**Fig. 5(d–f)**) collected in different representative regions denote characteristic VO_2(M) signatures in the VO_y(I) regions, i.e., V-$L_{2,3}$ white lines around 516 and 523 eV, respectively, and two peaks in the O-K pre-edge corresponding to the t_{2g} (about 528 eV) and e_g (about 531 eV). Within the VO_y(II) environment, the obtained spectra, although noisier, still return signals that are more consistent with the V^{4+} oxidation state. In addition, HRTEM micrographs (**Fig. 5(j–l)**) evidence the presence of interplanar distances associated with VO_2(M) in the VO_y(I) sublayers as well as the amorphous character of the most superficial regions.

Further STEM-EDX analyses (Supplementary Material Section II) not only demonstrate that W is homogeneously distributed throughout the thickness in the VO_y(I) layers, but also that the VO_y(II) regions are more depleted of this element. This could be associated with the W diffusion phenomenon that occurs during the RTA of the film. It has been previously revealed that oxidation within the reaction system used in the present work progresses from the surface to the substrate interface[40]. It is therefore expected that the surface of the sample will reach a given temperature more quickly. Higher temperatures lead to an increase in the diffusion rate of W into the film, which would explain the lower concentration of this element in the VO_y(II) overlayer. Likewise, tungsten, with a larger radius and an extra valence electron, could distort the crystalline structure of the VO_2(M) lattice formed on the surface as it diffuses into the VO_y(I) sublayer. Thus, the higher the concentration of dopant, the greater the overall amount of W that must diffuse and hence the thicker the overlying amorphous layer. This is in fine agreement with what was observed by XRD, explaining the progressive deterioration of crystallinity with doping. Obviously, and despite the fact that such a layer apparently has a stoichiometry of vanadium dioxide, the thicker the amorphous layer, the worse the thermochromic performance of the coating, since it should not be forgotten that the MIT transition is driven by the monoclinic-to-rutile structural phase change.

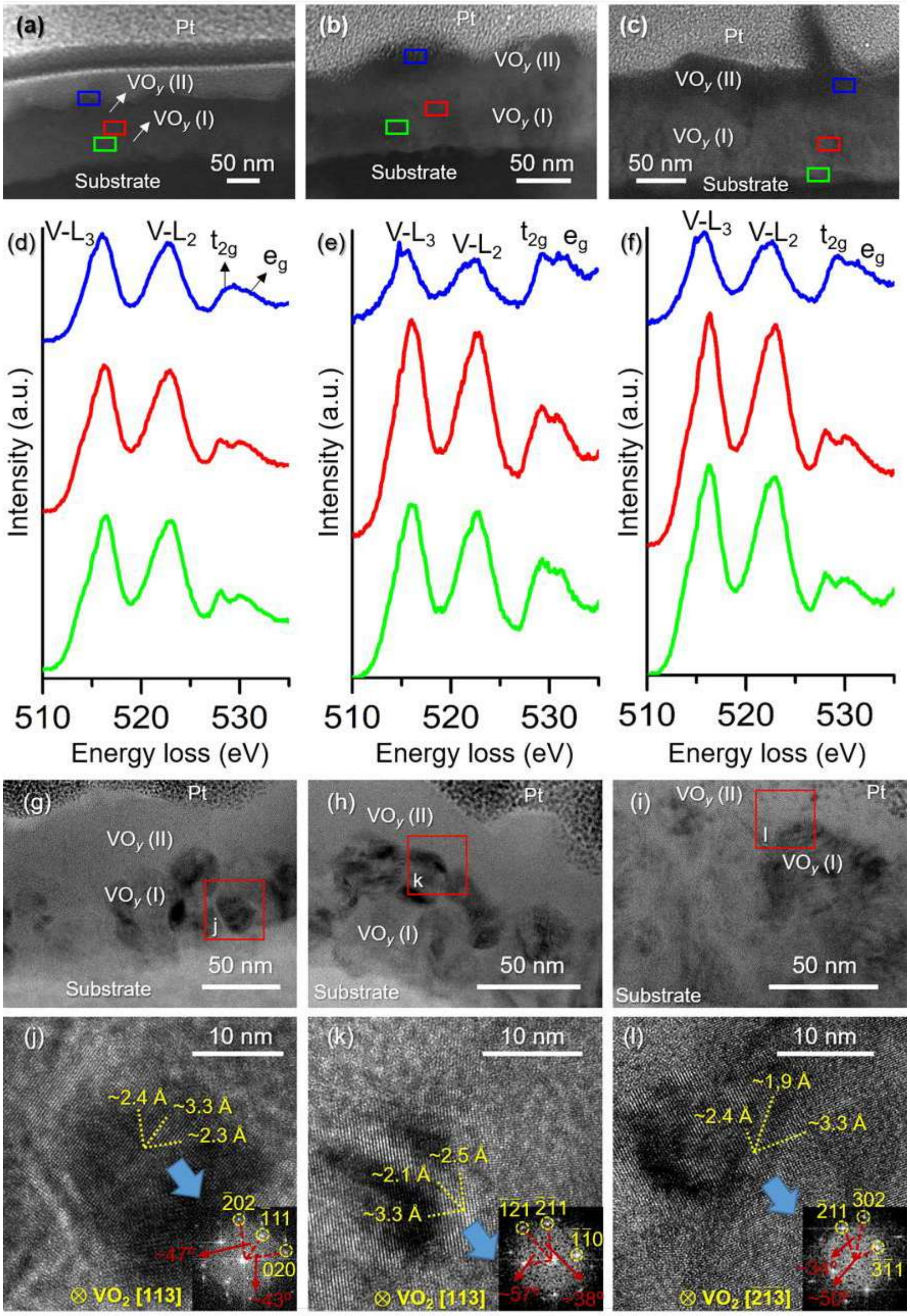

Figure 5. (S)TEM analyses performed on samples (left) 2W_T50_550_1, (center) 3W_T50_550_1, and (right) 5W_T50_475_30. (a–c) STEM-HAADF overviews. (d–f) Integrated EELS spectra corresponding to the areas marked in (a–c). (g–i) BF-TEM overviews. (j–l) HRTEM micrographs of the narrow regions highlighted in (g–i) together with their associated FFT spectra.

3.3. Optical characterization

Once the constitutive characteristics of the synthesized coatings have been identified, it is time to investigate the optical-thermochromic features that define their viability for application in smart glazing. For this purpose, Vis-NIR transmittance measurements (in the wavelength range between 350 and 2500 nm) were first conducted at 25 and 90ºC for all the samples addressed in this study. The values of the photometric (T_{lum}) and radiometric (T_{sol}, T_{IR}) parameters calculated from these results are shown in **Table 2**.

Table 2. Radiometric and photometric parameters changes upon heating for all the studied samples. For a detailed definition and explanation of how all these parameters are obtained, refer to the work by Outón *et al.* (Appendix A)[50]. The accuracy of these values is ±0.1%.

Sample	T_{lum} (%)	ΔT_{lum} (%)	ΔT_{sol} (%)	$\Delta T_{sol, rel}$ (%)	ΔT_{IR} (%)	$\Delta T_{IR, rel}$ (%)
1W_T50_475_30	39.6	3.7	7.2	19.9	12.6	32.0
1W_T50_550_1	45.5	2.8	5.3	13.4	10.6	24.8
1W_T25_475_10	50.2	-0.9	2.8	5.8	7.8	14.9
1W_T25_500_1	50.9	-1.1	2.9	5.7	8.1	14.5
2W_T50_475_30	39.4	2.2	5.8	15.9	10.4	26.0
2W_T50_550_1	49.2	3.8	5.0	12.4	8.4	20.5
2W_T25_475_10	51.3	0.9	3.9	7.9	8.5	15.5
2W_T25_500_1	49.1	0.9	4.7	9.3	10.6	18.6
3W_T50_475_30	51.7	3.5	4.4	10.8	6.9	17.6
3W_T50_550_1	52.0	3.2	5.2	12.4	9.1	21.6
3W_T37.5_525_1	47.8	2.7	4.4	10.9	8.0	19.4
3W_T25_475_10	58.0	0.3	2.5	4.5	5.3	9.4
3W_T25_500_1	64.4	1.9	2.4	4.1	3.5	5.8
5W_T50_475_30	37.2	2.0	4.1	12.8	7.2	22.1

On the one hand, **Figure 6** shows the results obtained for samples of 50 nm nominal layer thickness. In general, it can be seen that, for RTAs at 475ºC and 30 s, the luminous transmittance of the coatings increases among 1W, 2W and 3W. However, it seems that higher ratios lead to a noticeable decrease in this parameter (drop from 51.7% to 37.2% for 3W and 5W, respectively). A reasonably similar trend is also observed for samples subjected to instantaneous annealing at 550ºC, although with considerably higher values for 1W and 2W (T_{lum} of 45.5% and 49.2%, respectively). These behaviors are somewhat related to what has been seen previously by SEM/TEM: increasing doping up to 3W gives rise to progressively more defined grains with homogeneous textures, which translates into rises in T_{lum}. On the contrary, excessive doping leads to more heterogeneous structures with decreases in this parameter. In addition, a general and progressive reduction in absolute NIR transition amplitudes with temperature is evidenced for higher dopant concentrations, which was expected after the analysis of the GIXRD and (S)TEM results. The attenuation of the $\Delta T_{IR, rel}$ values, a parameter which has been previously used as a qualitative comparator of the VO_2(M) yields, also reflects this trend. In any case, these behaviors are expected in W-doped vanadium dioxide structures[23,28,51]. Nonetheless, it is worth mentioning that the T_{lum} and ΔT_{sol} pairs achieved here are relevant. Their values could be due to the effect that the inclusion of tungsten has in favoring a compact structure of homogeneous grains until reaching a maximum tungsten saturation ratio beyond which a worsening of the overall film performance occurs. In this context, it has been previously reported that the coexistence of VO_2(M) and V_2O_5 phases usually entails greater ΔT_{lum} values[37], which ultimately has a positive impact on the solar modulation ability of the coating. Hence the maintenance of ΔT_{sol} values always above 4% for this set of samples ($\Delta T_{lum} \geq 2\%$).

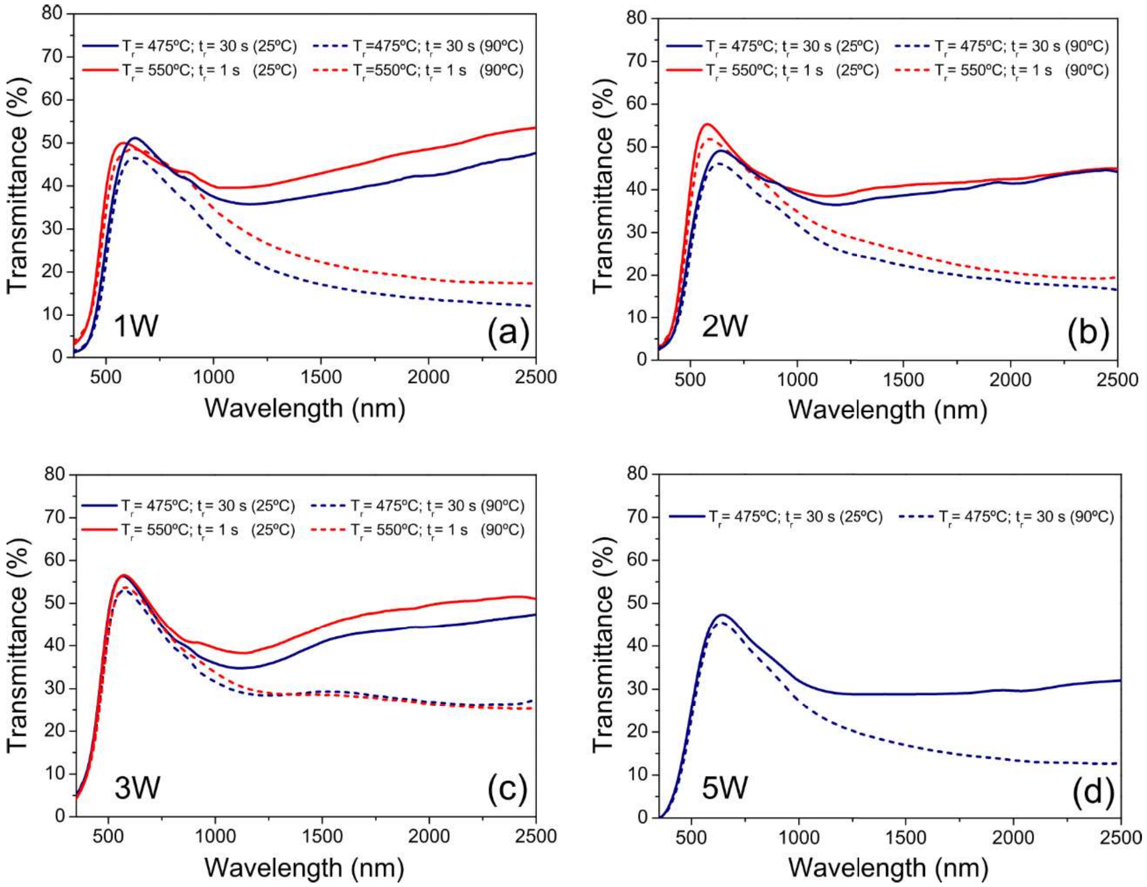

Figure 6. Vis-NIR transmittance spectra recorded at 25°C (solid lines) and 90°C (dashed lines) for 50 nm thick $V_xW_{1-x}O_2$-based coatings with increasing doping: (a) 1W, (b) 2W, (c) 3W, and (d) 5W. Samples were submitted to thermal annealing at 475°C for 60 s (blue lines) and 550°C for 1 s (red lines).

On the other hand, **Figure 7** collects the temperature-dependent optical responses for 25 nm thick samples. Overall, similar trends and behaviors are noticed for doped samples 1W and 2W, regardless of the applied thermal annealing conditions. However, further doping leads to increases, more pronounced for the sample subjected to instantaneous annealing at 500ºC, of the T_{lum} values (above 58%) although to the considerable detriment of those of ΔT_{sol} (below 3%). This suggests that the maximum saturation ratio for this thickness is lower than the one seen previously for 50 nm thick samples. That is, 2W, for which the best records of the T_{lum} and ΔT_{sol} pairs are accomplished (51.3 and 3.9, respectively for sample 2W_T25_475_10; and 49.1 and 4.7, respectively for 2W_T25_500_1). Moreover, the ΔT_{lum} values for these samples, which are sometimes even negative, lead us to think that they present heterogeneous morphologies and structures. This could be due to the initial GLAD structure achieved for layer thicknesses around 25 nm, which entails a growth regime mainly dominated by diffusive events resulting in nanostructures of limited porosity[38]. This promotes that, during thermal annealing, there are areas more prone/exposed to oxidation than others. Even so, such ΔT_{lum} values would also denote the absence of vanadium pentoxide. Since the above results do not improve those attained on 50 nm thick samples, it was decided to investigate an intermediate layer thickness to verify if further improvements could be achieved. However, the transmittance measurements at variable temperatures collected for sample 3W_T37.5_525_1 (Supplementary Material Section III) also revealed no significant enhancements over those of sample 3W_T50_550_1, which is the one that presents a better balance of T_{lum} and ΔT_{sol} maintained for a higher doping ratio.

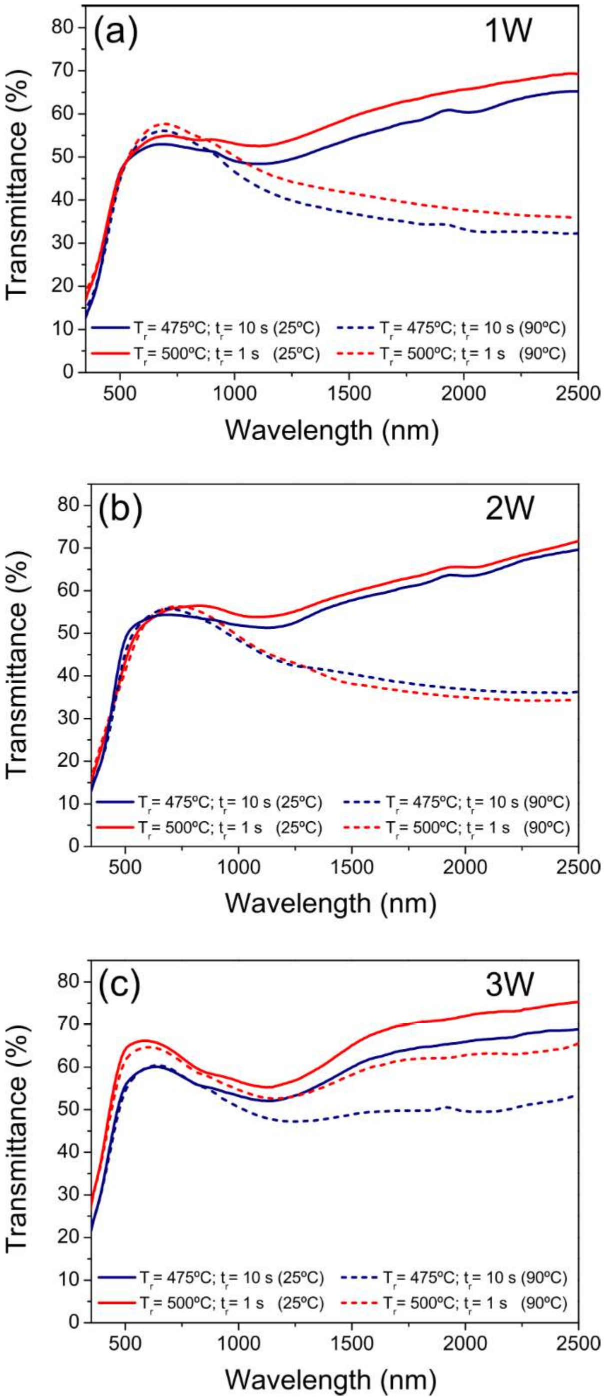

Figure 7. Vis-NIR transmittance spectra recorded at 25°C (solid lines) and 90°C (dashed lines) for 25 nm thick $V_xW_{1-x}O_2$-based coatings for (a) 1W, (b) 2W, and (c) 3W. Samples were submitted to thermal annealing at 475°C for 10 s (blue lines) and 500°C for 1 s (red lines).

For a comprehensive examination of the optical MIT hysteresis associated with each of the above samples, as well as for the determination of the T_c, the kinetic variation of transmittance at a fixed wavelength of 2000 nm was studied for consecutive heating-cooling cycles between 15–90ºC (**Figure 8** and **Figure 9**). In addition, the values of the parameters linked to the hysteresis features are listed in **Table 3**. The transition temperatures are calculated from the derivative curves of the transmittance *vs.* temperature plots with Gaussian fits (**Fig. 8 (b–e)(g–i)** and **Fig. 9(b–c)(e–f)**). The hysteresis smoothness (S_H), defined as the temperature range for which 65–75% of the total transmittance drop at 2000 nm occurs, is given by the average full width at half maximum (FWHM) of the derivatives for each heating and cooling cycle. **Fig. 8** illustrates the hysteresis loops recorded for samples with a nominal thickness of 50 nm. As expected, a progressive lowering in T_c is achieved as the W concentration increases, which confirms the success of the methodologies proposed for effective VO_2(M) doping. More specifically, samples oxidized at 475ºC for 30 s (**Fig. 8(a–e)**) experience a decrease in T_c during heating cycles from 56ºC to 37ºC for doping levels between those of 1W and 5W. Similarly, reductions in W_H are observed as doping increases, although always within a fairly narrow range of 10–14ºC. In terms of VO_2(M) yields, the ΔT_{rel} values reveal analogous results for this group of samples, suggesting that their gradual decline in the solar modulation ability (as shown in **Table 2**) is mainly associated with the presence of tungsten (a common pattern in W-doped coatings). It is also noted that, in contrast to previous studies on undoped samples subjected to the same annealing[39], the inclusion of W leads to the development of nearly symmetrical hysteresis, with transitions occurring in single steps during each of the heating and cooling stages (i.e., a single peak in the derivatives). This effect, as well as the progressive increase in S_H

(from 12ºC to 26ºC between 1W and 5W), are also attributable, as observed in the literature[21,25,46], to the inclusion of W in the lattice structure of VO_2(M).

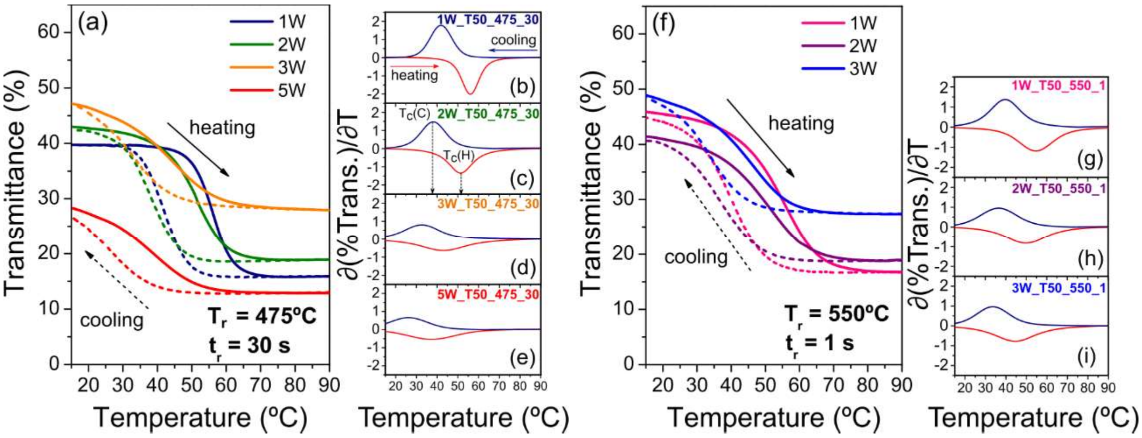

Figure 8. Thermal evolution of the optical transmittance at 2000 nm recorded during consecutive heating (solid lines) and cooling (dashed lines) cycles together with their associated derivatives (red and blue lines, respectively) for 50 nm thick $V_xW_{1-x}O_2$-based coatings synthesized at (a–e) 475 °C for 30 s, and (f–i) 550 °C for 1 s. For a better overview, the cooling derivatives are represented in absolute values.

On the other hand, similar trends, although less pronounced in terms of S_H, are also observed for samples subjected to instantaneous annealing at 550ºC (**Fig. 8 (f–i)**). It seems that, although the application of either thermal treatment has no substantial impact on the T_c reached, instantaneous annealing drives to the development of more gradual phase changes (S_H = 20–24ºC) regardless of the doping level. This is related to the fact that this kind of treatment results in growth-limited (high density of grain boundaries) and oxygen-deficient structures[37,38], which can act as barriers, slowing down the development of the MIT transition in both directions, in the same way as would occur by the inclusion of W in ascending quantities. Furthermore, and in contrast to what was previously observed, ΔT_{rel} values progressively decrease in the direction 1W, 2W, 3W. However, this a priori decrease in VO_2(M) performance does not have a direct and significant impact on the final ΔT_{sol} values (between 5.0–5.3% for samples 1W–3W_T50_550_1). It is therefore confirmed that flash annealing somewhat dampens the adverse effects that the inclusion of tungsten normally has on the solar modulation ability without apparently affecting T_c. This comes at the cost of the development of more progressive transitions even at lower doping.

Table 3. Main features of the thermochromic hysteresis loops of all the studied samples. T_c denotes the temperatures of the MIT transition on heating; W_H is the hysteresis loop width given by the differences of the MIT temperatures on heating and cooling cycles; ΔT_{rel} is the relative decrease of transmittance upon the transition at 2000 nm; and S_H is the hysteresis smoothness. The accuracy of temperature and transmittance values are ±0.5ºC and ±0.1%, respectively.

Sample	**T_c (ºC)**	**W_H (ºC)**	**ΔT_{rel} (%)**	**S_H (ºC)**
1W_T50_475_30	56	14	59.9	12
1W_T50_550_1	55	15	63.5	20
1W_T25_475_10	56	19	39.0	14
1W_T25_500_1	48	13	45.0	14
2W_T50_475_30	51	13	56.0	16
2W_T50_550_1	50	14	54.4	23
2W_T25_475_10	48	13	47.9	16
2W_T25_500_1	48	13	45.3	15
3W_T50_475_30	43	10	40.9	24
3W_T50_550_1	44	10	44.3	22
3W_T37.5_525_1	43	10	48.3	29
5W_T50_475_30	37	11	54.6	26

Finally, **Fig. 9** shows the thermochromic features of samples with a nominal layer thickness of 25 nm doped at 1W and 2W. It should be noted that the kinetic variation of the transmittance was not measured for samples 3W_T25_475_10 and 3W_T25_500_1 as a consequence of their previous results. In principle, symmetrical hystereses are again visible, all of them with quite similar values of T_c, W_H, ΔT_{rel} and S_H, except for sample 1W_T25_475_10, which has a hysteresis 6ºC wider than the others. In fact, this sample is the one with a substantially higher T_c (56ºC compared to 48ºC calculated for the rest of the 25 nm sample). It is also worth recalling the rather limited ΔT_{sol} performances reached for both the aforementioned sample as well as for 1W_T25_500_1, which were initially associated with their negative ΔT_{lum} values (see **Table 2**). The above, coupled with the discrete outcomes for samples 2W, lead us to think that this layer thickness is not the most adequate in relation to the proposed synthesis and doping strategies. Also, although the T_c lowering are considerable, they are not enough to justify the simultaneous deterioration of T_{lum} and ΔT_{sol} with respect to those previously achieved in undoped samples[39]. The same applies to sample 3W_T37.5_525_1 (see Supplementary Material Section III), which also exhibited no significant improvement in T_c over other samples of equivalent dopant ratio.

In light of all the above, it can be concluded that the best results are obtained for coatings of 50 nm nominal layer thickness, more specifically for sample 3W_T50_550_1, which presents the best balance of T_{lum} (52.0%), ΔT_{sol} (5.2%) and T_c (44ºC). Nevertheless, although these performances are relatively moderate, it should be noted that they are conditioned by the maximum transmittance of the substrate used in this study (Tl_{um} = 82.1% and T_{sol} = 83.5% for bare glass). Therefore, if the negative effects coming from the substrate are neglected and only the contribution of the $V_xW_{1-x}O_2$ based films is evaluated (for more information, refer to Supplementary Material Section IV), the previous values of T_{lum} and ΔT_{sol} increase up to 63.4% and 6.2%, respectively, which are especially noteworthy considering that it is a (i) doped system

(ii) based on a single-layer approach. Indeed, these performances are not far from those sometimes resulting from complex VO_2(M)-containing multilayered designs[52].

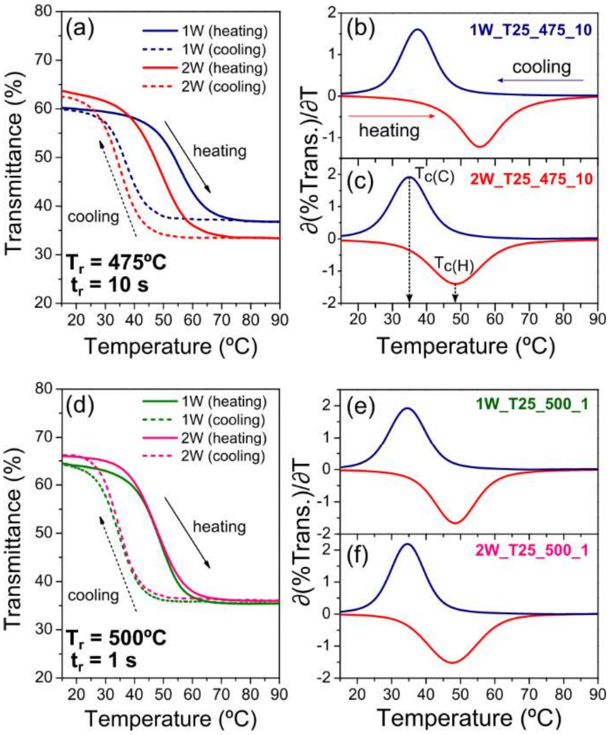

Figure 9. Thermal evolution of the optical transmittance at 2000 nm recorded during consecutive heating (solid lines) and cooling (dashed lines) cycles together with their associated derivatives (red and blue lines, respectively) for 25 nm thick $V_xW_{1-x}O_2$-based coatings synthesized at (a–b) 475 °C for 10 s, and (d–e) 500 °C for 1 s. For a better overview, the cooling derivatives are represented in absolute values.

At this stage, it is time to question whether the manufactured coatings would have real-life applicability. This is where W_H and S_H come into play, as well as other factors such as geographical location and/or orientation of the glazing. In other words, the requirements of a glass continuously or partially exposed to direct solar radiation cannot, under any circumstance, be the same as those of glass that receives radiation indirectly. In the first example, the glazing surface absorbs much of the incident radiation allowing it to reach, in relatively short periods of time, temperatures 10–15ºC above that of the environment[53]. Thus, T_c between 35–45°C would be appropriate for coatings operating under these conditions. However, their applicability would be restricted to wide hysteresis, which are necessary to keep the thermal blocking active after the cessation of radiation up to temperatures of about 25–30°C. On the contrary, a shaded glass, which would receive indirect radiation, will ideally require T_c closer to 25°C as well as narrower W_H values. In terms of S_H, it is generally desirable for state changes to occur gradually, which also leads to greater comfort. In any case, the requirements for this parameter will always be superior the higher the MIT temperature, since this would allow an earlier activation of the heat blocking.

All things considered, it is thought to be undesirable to idealize a standard/universal design of smart glazing, but rather it should be adapted to specific circumstances beyond those described above (weather conditions, installation in a static system, such as a building, or a dynamic system, like a car, etc.). This is why, based on the above arguments, it is considered that sample 3W_T50_550_1 could have potential application on glazed surfaces exposed to temperatures between 30–35ºC during the warmer seasons and receiving continuously or partially direct solar radiation. However, this current design can still be improved not only in terms of thermochromic performance, for instance by implementing multilayered or graded-index antireflective approaches based on oxides with high visible transmittance and chemical stability (SiO_2, TiO_2, ZrO_2, or even V_2O_5), but also by providing additional functionalities, such as durability and/or self-cleaning (i.e. hydrophobicity). Hence, it is necessary to continue researching both the development of new designs as well as the exploration of other dopants, either alone or in combination with others, with the aim of providing coatings with specific characteristics that make them more appropriate for application in a given work environment.

4. Conclusions

The success of a new approach to the fabrication of 25 and 50 nm thick $V_xW_{1-x}O_2$ coatings on glass substrates by DC magnetron co-sputtering of vanadium and tungsten combined with GLAD and RGPP processes and subsequent rapid thermal annealing in an air atmosphere has been demonstrated. Limitations encountered during the deposition stages to reach dopant concentrations lower than for 15W-type samples led to the adoption of additional strategies based on the fabrication of alternating $VO_y/V_{0.85}W_{0.15}O_y$ multilayers. By modulating the thickness and number of these layers, aimed dopant percentages between those of samples 1W–5W were achieved. GIXRD and (S)TEM investigations evidenced the effective synthesis of thermochromic $V_xW_{1-x}O_2$-based coatings after thermal annealing. However, a deterioration of the crystallinity with increasing dopant percentage was also demonstrated, which in turn was related to the appearance of increasingly thicker amorphous layers on the surface apparently preserving the V^{4+} oxidation state. Optical characterizations revealed significant and progressive decreases in T_c as tungsten concentration increases, although at the expense of noticeable depletions of either T_{lum} or ΔT_{sol}, as expected from doping. SEM investigations on 50 nm thick samples demonstrated the development of characteristic VO_2(M) microstructures consisting of increasingly larger and more homogeneous grains for doping up to that of 3W, which resulted in direct improvements of luminous transmittances. On the contrary, higher percentages resulted in more heterogeneous morphologies leading to simultaneous deteriorations of T_{lum} and ΔT_{sol}. Furthermore, it was also shown that higher doping gives rise to progressive narrowing of the hysteresis, although always with W_H values $\geq$ 10ºC.

Overall, it was determined that the proposed methodologies are more suitable for 50 nm thick samples subjected to instantaneous annealing at 550ºC, which allows to mitigate, up to a maximum tungsten percentage (that of 3W), the adverse effects that the inclusion of dopant has on T_{lum} and ΔT_{sol} (values of 52.0% and 5.2%, respectively, were calculated for the sample 3W_T50_550_1) while attaining a T_c during heating of 44ºC. The above features, coupled with W_H and S_H values of 10ºC and 22ºC, respectively, make this coating potentially applicable as smart glazing directly exposed to solar radiation.

Acknowledgements

A. J. Santos would like to thank the University of Cádiz and the Spanish Ministerio de Universidades for the concession of a “Margarita Salas” postdoctoral fellowship funded by the European Union - NextGenerationEU (2021-067#9663/PN/MS-RECUAL/CD). University of Cádiz and IMEYMAT are also acknowledged by financing the mutual facilities available at the UCA R&D Central Services (SC-ICYT), the UCA project reference “PUENTE PR2022-027”, and the IMEYMAT project reference “LÍNEAS PRIORITARIAS PLP2021120-1”. This work was supported by the Spanish State R&D projects (Retos y Generación de Conocimiento) with references PID2020–114418RBI00 and PID2023-150975OB-I00. J. J. Jiménez and A. Casas-Acuña also acknowledge Spanish Ministry of Science and Innovation for the granting of postdoctoral and predoctoral contracts, respectively, within the framework of the project Ref. PID2020–114418RBI00. This work was partly supported by the French

RENATECH network, FEMTO-ST technological facility, by the Region Bourgogne-Franche-Comté and by EIPHI Graduate School (Contract “ANR–17–EURE–0002”).

Data availability statement

Data will be made available on request.

Declaration of Competing Interest

The authors declare that they have no known competing financial interests or personal relationships that could have appeared to influence the work reported in this paper.

REFERENCES

[1] K. Khaled, U. Berardi, Current and future coating technologies for architectural glazing applications, Energy Build. 244 (2021) 111022. doi:10.1016/j.enbuild.2021.111022.

[2] A. Roy, A. Ghosh, T.K. Mallick, A.A. Tahir, Smart glazing thermal comfort improvement through near-infrared shielding paraffin incorporated SnO_2-Al_2O_3 composite, Constr. Build. Mater. 331 (2022) 127319. doi:10.1016/j.conbuildmat.2022.127319.

[3] M. Aburas, V. Soebarto, T. Williamson, R. Liang, H. Ebendorff-Heidepriem, Y. Wu, Thermochromic smart window technologies for building application: A review, Appl. Energy. 255 (2019) 113522. doi:10.1016/j.apenergy.2019.113522.

[4] S. Wu, H. Sun, M. Duan, H. Mao, Y. Wu, H. Zhao, B. Lin, Applications of thermochromic and electrochromic smart windows: Materials to buildings, Cell Reports Phys. Sci. 4 (2023) 101370. doi:10.1016/j.xcrp.2023.101370.

[5] S.D. Rezaei, S. Shannigrahi, S. Ramakrishna, A review of conventional, advanced, and smart glazing technologies and materials for improving indoor environment, Sol. Energy Mater. Sol. Cells. 159 (2017) 26–51. doi:10.1016/j.solmat.2016.08.026.

[6] A. Ghosh, R. Hafnaoui, A. Mesloub, K. Elkhayat, G. Albaqawy, M.M. Alnaim, M.S. Mayhoub, Active smart switchable glazing for smart city: A review, J. Build. Eng. 84 (2024) 108644. doi:10.1016/j.jobe.2024.108644.

[7] Y. Cui, Y. Ke, C. Liu, Z. Chen, N. Wang, L. Zhang, Y. Zhou, S. Wang, Y. Gao, Y. Long, Thermochromic VO_2 for Energy-Efficient Smart Windows, Joule. 2

(2018) 1707–1746. doi:10.1016/j.joule.2018.06.018.

[8] N. Shen, S. Chen, R. Huang, J. Huang, J. Li, R. Shi, S. Niu, A. Amini, C. Cheng, Vanadium dioxide for thermochromic smart windows in ambient conditions, Mater. Today Energy. 21 (2021) 100827. doi:10.1016/j.mtener.2021.100827.

[9] X. Cao, T. Chang, Z. Shao, F. Xu, H. Luo, P. Jin, Challenges and Opportunities toward Real Application of VO_2-Based Smart Glazing, Matter. 2 (2020) 862–881. doi:10.1016/j.matt.2020.02.009.

[10] S. Wang, T. Jiang, Y. Meng, R. Yang, G. Tan, Y. Long, Scalable thermochromic smart windows with passive radiative cooling regulation, Science. 374 (2021) 1501–1504. doi:10.1126/science.abg0291.

[11] X. Li, C. Cao, C. Liu, W. He, K. Wu, Y. Wang, B. Xu, Z. Tian, E. Song, J. Cui, G. Huang, C. Zheng, Z. Di, X. Cao, Y. Mei, Self-rolling of vanadium dioxide nanomembranes for enhanced multi-level solar modulation, Nat. Commun. 13 (2022) 7819. doi:10.1038/s41467-022-35513-w.

[12] J.-P. Pouget, Basic aspects of the metal–insulator transition in vanadium dioxide VO_2: A critical review, Comptes Rendus Phys. 22 (2021) 37–87. http://dx.doi.org/10.1016/j.crhy.2014.06.003.

[13] H. Lu, S. Clark, Y. Guo, J. Robertson, The metal-insulator phase change in vanadium dioxide and its applications, J. Appl. Phys. 129 (2021) 240902. doi:10.1063/5.0027674.

[14] J.B. Goodenough, The two components of the crystallographic transition in VO_2, J. Solid State Chem. 3 (1971) 490–500. doi:10.1016/0022-4596(71)90091-0.

[15] S.Y. Li, G.A. Niklasson, C.G. Granqvist, Thermochromic fenestration with VO_2-

based materials: Three challenges and how they can be met, Thin Solid Films. 520 (2012) 3823–3828. doi:10.1016/j.tsf.2011.10.053.

[16] S. Wang, M. Liu, L. Kong, Y. Long, X. Jiang, A. Yu, Recent progress in VO_2 smart coatings: Strategies to improve the thermochromic properties, Prog. Mater. Sci. 81 (2016) 1–54. doi:10.1016/j.pmatsci.2016.03.001.

[17] M.G. Krishna, Y. Debauge, A.K. Bhattacharya, X-ray photoelectron spectroscopy and spectral transmittance study of stoichiometry in sputtered vanadium oxide films, Thin Solid Films. 312 (1998) 116–122. doi:10.1016/s0040-6090(97)00717-7.

[18] A. Perucchi, L. Baldassarre, P. Postorino, S. Lupi, Optical properties across the insulator to metal transitions in vanadium oxide compounds, J. Phys. Condens. Matter. 21 (2009) 323202. doi:10.1088/0953-8984/21/32/323202.

[19] E. Hryha, E. Rutqvist, L. Nyborg, Stoichiometric vanadium oxides studied by XPS, Surf. Interface Anal. 44 (2012) 1022–1025. doi:10.1002/sia.3844.

[20] Y.-B. Kang, Critical Evaluation and Thermodynamic Optimization of the VO–$VO_{2.5}$ System, J. Eur. Ceram. Soc. 32 (2012) 3187–3198. doi:10.1007/s11663-020-01939-0.

[21] S. Dou, W. Zhang, Y. Wang, Y. Tian, Y. Wang, X. Zhang, L. Zhang, L. Wang, J. Zhao, Y. Li, A facile method for the preparation of W-doped VO_2 films with lowered phase transition temperature, narrowed hysteresis loops and excellent cycle stability, Mater. Chem. Phys. 215 (2018) 91–98. doi:10.1016/j.matchemphys.2018.05.018.

[22] T.D. Vu, H. Xie, S. Wang, J. Hu, X. Zeng, Y. Long, Durable vanadium dioxide

with 33-year service life for smart windows applications, Mater. Today Energy. 26 (2022) 100978. doi:10.1016/j.mtener.2022.100978.

[23] B. Li, S. Tian, H. Tao, X. Zhao, Tungsten doped M-phase VO_2 mesoporous nanocrystals with enhanced comprehensive thermochromic properties for smart windows, Ceram. Int. 45 (2019) 4342–4350. doi:10.1016/j.ceramint.2018.11.109.

[24] H. Yang, S. Lee, C. Ko, Tungsten-doped vanadium dioxide thin film synthesis by alternate layer-by-layer growth and post-deposition annealing, Mater. Lett. 262 (2020) 127081. doi:10.1016/j.matlet.2019.127081.

[25] J. Luo, M. Gong, S. Tian, L. Zhou, T. Zheng, X. Zhao, B. Liu, Electrical and optical properties of highly crystalline W-VO_2 nano-films prepared by thermal oxidation of V-WO_3 precursors, Jpn. J. Appl. Phys. 62 (2023) 015505. doi:10.35848/1347-4065/acae68.

[26] H. Zong, H. Chen, L. Bian, B. Sun, Y. Yin, C. Zhang, W. Qiao, L. Yan, Q. Hu, M. Li, An approach for obtaining thermochromic smart windows with excellent performance and low phase transition temperature based on VO_2/tungsten-doped VO_2/VO_2 composite structure, Infrared Phys. Technol. 137 (2024) 105186. doi:10.1016/j.infrared.2024.105186.

[27] M. Kong, K. Egbo, C.P. Liu, M.K. Hossain, C.Y. Tso, C.Y. Hang Chao, K.M. Yu, Rapid thermal annealing assisted facile solution method for tungsten-doped vanadium dioxide thin films on glass substrate, J. Alloys Compd. 833 (2020) 155053. doi:10.1016/j.jallcom.2020.155053.

[28] A.E. Ersundu, M. Çelikbilek Ersundu, E. Doğan, M.B. Güven, A comparative investigation on thermal, structural and optical properties of W and Nb-doped VO_2-based thermochromic thin films, Thin Solid Films. 700 (2020) 137919.

doi:10.1016/j.tsf.2020.137919.

[29] Z. Zhao, D. Li, J. Yang, J. Li, H. Jin, Metal-insulator transition tuned by valence variation of Nb dopants in Nb-doped VO_2 films, Appl. Surf. Sci. 635 (2023) 157705. doi:10.1016/j.apsusc.2023.157705.

[30] X. Lv, X. Chai, L. Lv, Y. Cao, Y. Zhang, L. Song, Preparation of porous Mo-doped VO_2 films via atomic layer deposition and post annealing, Jpn. J. Appl. Phys. 60 (2021) 085501. doi:10.35848/1347-4065/ac1038.

[31] S. Amador-Alvarado, J.M. Flores-Camacho, A. Solís-Zamudio, R. Castro-García, J.S. Pérez-Huerta, E. Antúnez-Cerón, J. Ortega-Gallegos, J. Madrigal-Melchor, V. Agarwal, D. Ariza-Flores, Temperature-dependent infrared ellipsometry of Mo-doped VO_2 thin films across the insulator to metal transition, Sci. Rep. 10 (2020) 8555. doi:10.1038/s41598-020-65279-4.

[32] T.C. Chang, X. Cao, S.H. Bao, S.D. Ji, H.J. Luo, P. Jin, Review on thermochromic vanadium dioxide based smart coatings: from lab to commercial application, Adv. Manuf. 6 (2018) 1–19. doi:10.1007/s40436-017-0209-2.

[33] L. Hu, H. Tao, G. Chen, R. Pan, M. Wan, D. Xiong, X. Zhao, Porous W-doped VO_2 films with simultaneously enhanced visible transparency and thermochromic properties, J. Sol-Gel Sci. Technol. 77 (2016) 85–93. doi:10.1007/s10971-015-3832-z.

[34] L. Pósa, G. Molnár, B. Kalas, Z. Baji, Z. Czigány, P. Petrik, J. Volk, A rational fabrication method for low switching-temperature VO_2, Nanomaterials. 11 (2021) 212. doi:10.3390/nano11010212.

[35] P. Ashok, Y.S. Chauhan, A. Verma, Effect of vanadium thickness and deposition

temperature on VO_2 synthesis using atmospheric pressure thermal oxidation, Thin Solid Films. 724 (2021) 138630. doi:10.1016/j.tsf.2021.138630.

[36] Y. Zhan, X. Xiao, Y. Lu, Z. Cao, S. Qi, C. Huan, C. Ye, H. Cheng, J. Shi, X. Xu, G. Xu, The growth mechanism of VO_2 multilayer thin films with high thermochromic performance prepared by RTA in air, Surf. Interfaces. 9 (2017) 173–181. doi:10.1016/j.surfin.2017.09.002.

[37] A.J. Santos, N. Martin, J. Outón, E. Blanco, R. García, F.M. Morales, A simple two-step approach to the fabrication of VO_2-based coatings with unique thermochromic features for energy-efficient smart glazing, Energy Build. 285 (2023) 112892. doi:10.1016/j.enbuild.2023.112892.

[38] A.J. Santos, N. Martin, J. Outón, E. Blanco, R. García, F.M. Morales, Towards the optimization of a simple route for the fabrication of energy-efficient VO_2-based smart coatings, Sol. Energy Mater. Sol. Cells. 254 (2023) 112253. doi:10.1016/j.solmat.2023.112253.

[39] A.J. Santos, N. Martin, J.J. Jiménez, R. García, F.M. Morales, Enhancing luminous transmittance and hysteresis width of VO_2-based thermochromic coatings by combining GLAD and RGPP approaches, Constr. Build. Mater. 419 (2024) 135472. doi:10.1016/j.conbuildmat.2024.135472.

[40] A.J. Santos, B. Lacroix, M. Domínguez, R. García, N. Martin, F.M. Morales, Controlled grain-size thermochromic VO_2 coatings by the fast oxidation of sputtered vanadium or vanadium oxide films deposited at glancing angles, Surf. Interfaces. 27 (2021) 101581. doi:10.1016/j.surfin.2021.101581.

[41] N. Fairley, V. Fernandez, M. Richard-Plouet, C. Guillot-Deudon, J. Walton, E. Smith, D. Flahaut, M. Greiner, M. Biesinger, S. Tougaard, D. Morgan, J.

Baltrusaitis, Systematic and collaborative approach to problem solving using X-ray photoelectron spectroscopy, Appl. Surf. Sci. Adv. 5 (2021) 100112. doi:10.1016/j.apsadv.2021.100112.

[42] Z. Huang, Z. Wu, C. Ji, J. Dai, Z. Xiang, D. Wang, X. Dong, Y. Jiang, Improvement of phase transition properties of magnetron sputtered W-doped VO_2 films by post-annealing approach, J. Mater. Sci. Mater. Electron. 31 (2020) 4150–4160. doi:10.1007/s10854-020-02964-0.

[43] A. Kumar, A. Kumar, A. Kandasami, V.R. Singh, A Comprehensive Review on Synthesis, Phase Transition, and Applications of VO_2, J. Supercond. Nov. Magn. 37 (2024) 475–498. doi:10.1007/s10948-024-06705-w.

[44] M.M. Margoni, S. Mathuri, K. Ramamurthi, R.R. Babu, K. Sethuraman, Sprayed vanadium pentoxide thin films: Influence of substrate temperature and role of HNO_3 on the structural, optical, morphological and electrical properties, Appl. Surf. Sci. 418 (2017) 280–290. doi:10.1016/j.apsusc.2017.02.039.

[45] A. Baltakesmez, C. Aykaç, B. Güzeldir, Phase transition and changing properties of nanostructured V_2O_5 thin films deposited by spray pyrolysis technique, as a function of tungsten dopant, Appl. Phys. A Mater. Sci. Process. 125 (2019) 441. doi:10.1007/s00339-019-2736-0.

[46] D.U. Singh, R. Narayanan, Temperature tunable flexible photo absorbers based on near-infrared 1D photonic crystal hybridized W-doped VO_2 nanostructures, Nanotechnology. 33 (2022) 065204. doi:10.1088/1361-6528/ac33d4.

[47] H.M. Barra, S.K. Chen, N. Tamchek, Z.A. Talib, O.J. Lee, K.B. Tan, Phase, Microstructure, Thermochromic, and Thermophysical Analyses of Hydrothermally Synthesized W-Doped VO_2 Nanopowder, Adv. Mater. Sci. Eng.

2021 (2021) 582274,. doi:10.1155/2021/8582274.

[48] Y. Wu, L. Fan, W. Huang, S. Chen, S. Chen, F. Chen, C. Zou, Z. Wu, Depressed transition temperature of $W_xV_{1-x}O_2$: Mechanistic insights from the X-ray absorption fine structure (XAFS) spectroscopy, Phys. Chem. Chem. Phys. 16 (2014) 17705–17714. doi:10.1039/c4cp01661k.

[49] J. Outón, E. Blanco, M. Domínguez, H. Bakkali, J.M. Gonzalez-Leal, J.J. Delgado, M. Ramírez-del-Solar, Tracking the optical constants of porous vanadium dioxide thin films during metal–insulator transition: Influence of processing conditions on their application in smart glasses, Appl. Surf. Sci. 580 (2022) 152228. doi:10.1016/j.apsusc.2021.152228.

[50] L. Zhang, F. Xia, J. Yao, T. Zhu, H. Xia, G. Yang, B. Liu, Y. Gao, Facile synthesis, formation mechanism and thermochromic properties of W-doped VO_2(M) nanoparticles for smart window applications, J. Mater. Chem. C. 8 (2020) 13396–13404. doi:10.1039/d0tc03436c.

[51] J. Houska, Design and reactive magnetron sputtering of thermochromic coatings, J. Appl. Phys. 131 (2022) 110901. doi:10.1063/5.0084792.

[52] T. Palomar, E. Enríquez, Evaluation of the interaction of solar radiation with colored glasses and its thermal behavior, J. Non. Cryst. Solids. 579 (2022) 121376. doi:10.1016/j.jnoncrysol.2021.121376.

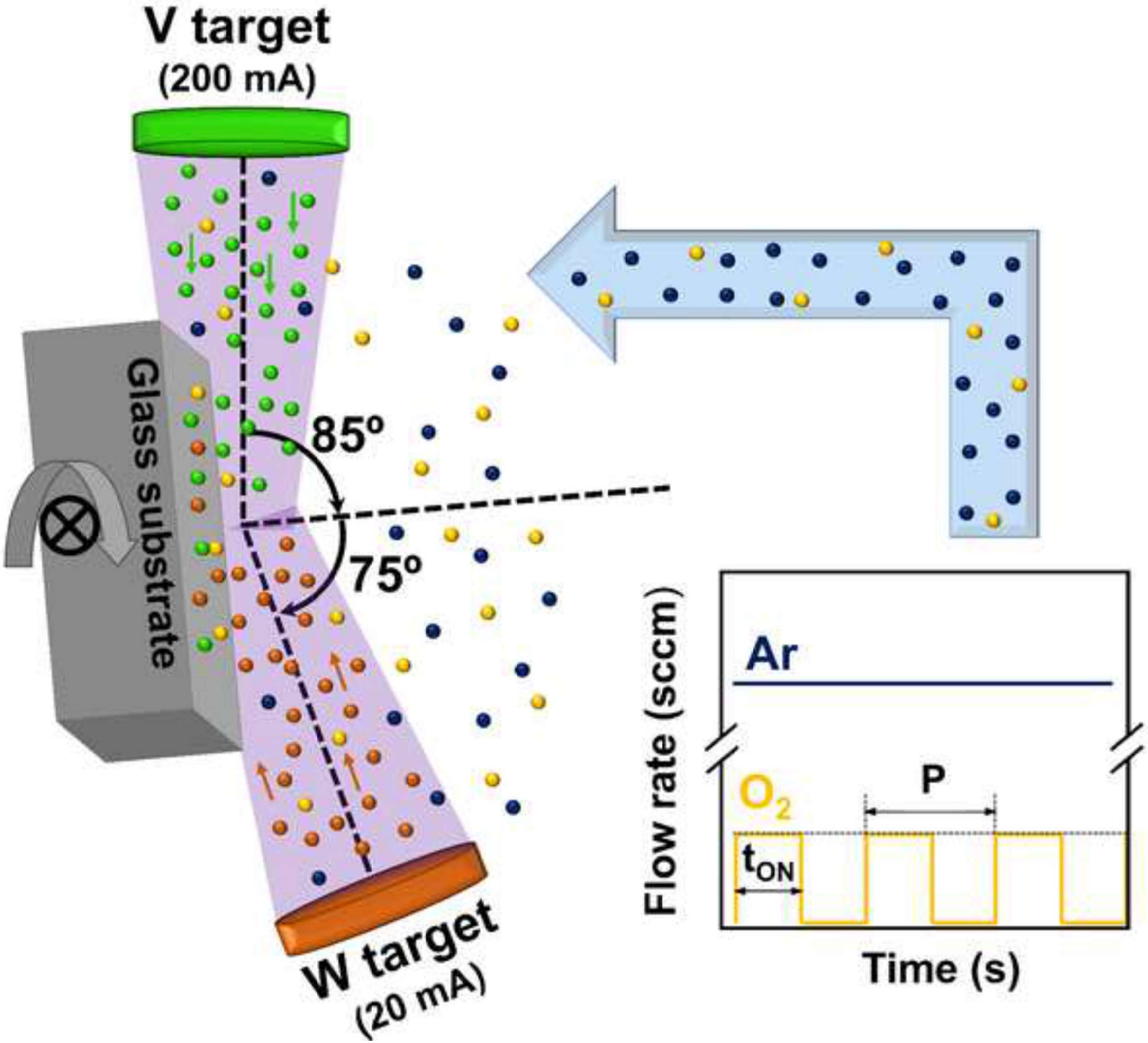
V target
(200 mA)
Glass substrate
85°
75°
W target
(20 mA)
Ar
O_2
t_{ON}
P
Flow rate (sccm)
Time (s)

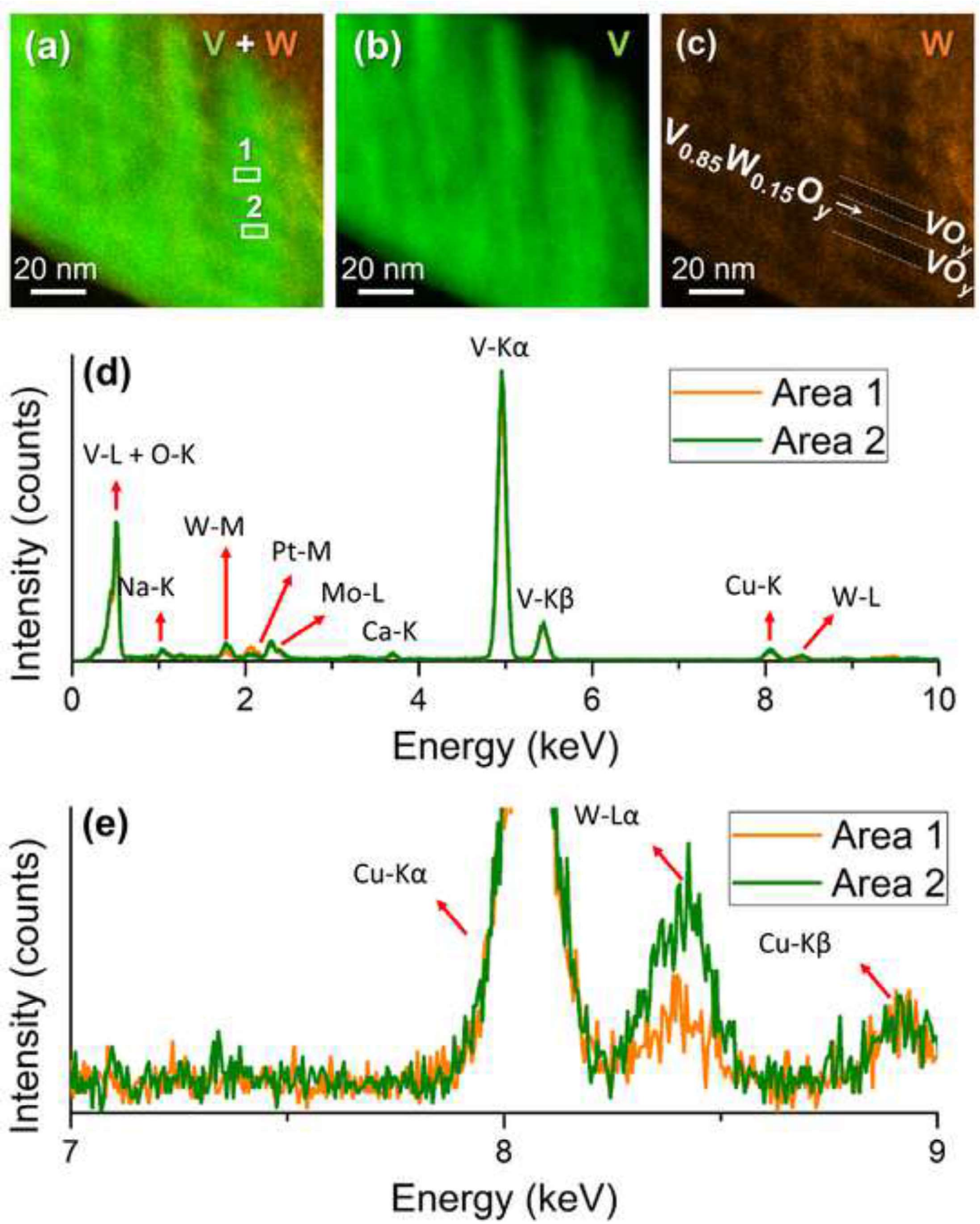
(a)
V + W
1
2
20 nm
(b)
V
20 nm
(c)
W
$V_{0.85}W_{0.15}O_y$
VO_y
VO_y
20 nm
(d)
Intensity (counts)
Energy (keV)
V-L + O-K
Na-K
W-M
Pt-M
Mo-L
Ca-K
V-Kα
V-Kβ
Cu-K
W-L
Area 1
Area 2
0
2
4
6
8
10
(e)
Intensity (counts)
Energy (keV)
Cu-Kα
W-Lα
Cu-Kβ
Area 1
Area 2
7
8
9

Figure 3

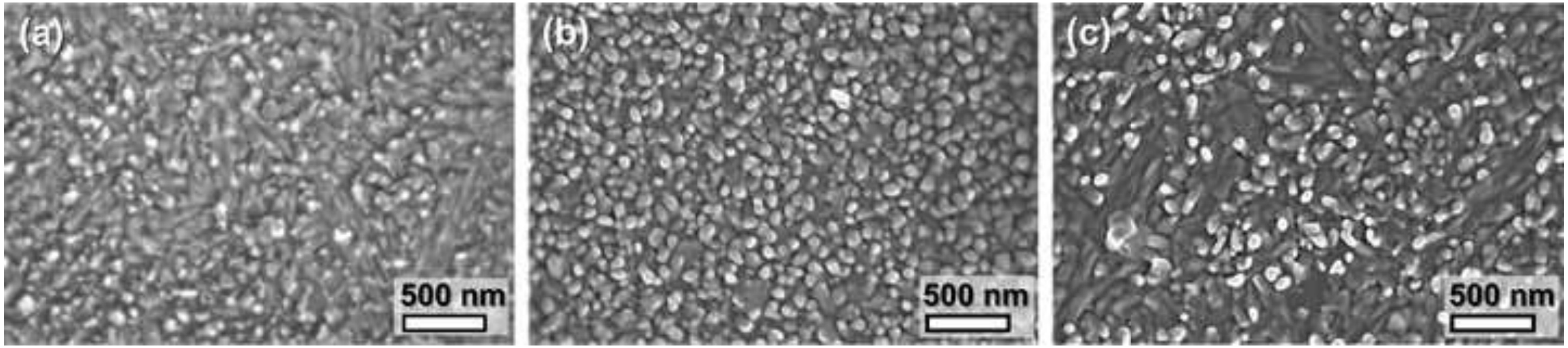

Figure 4

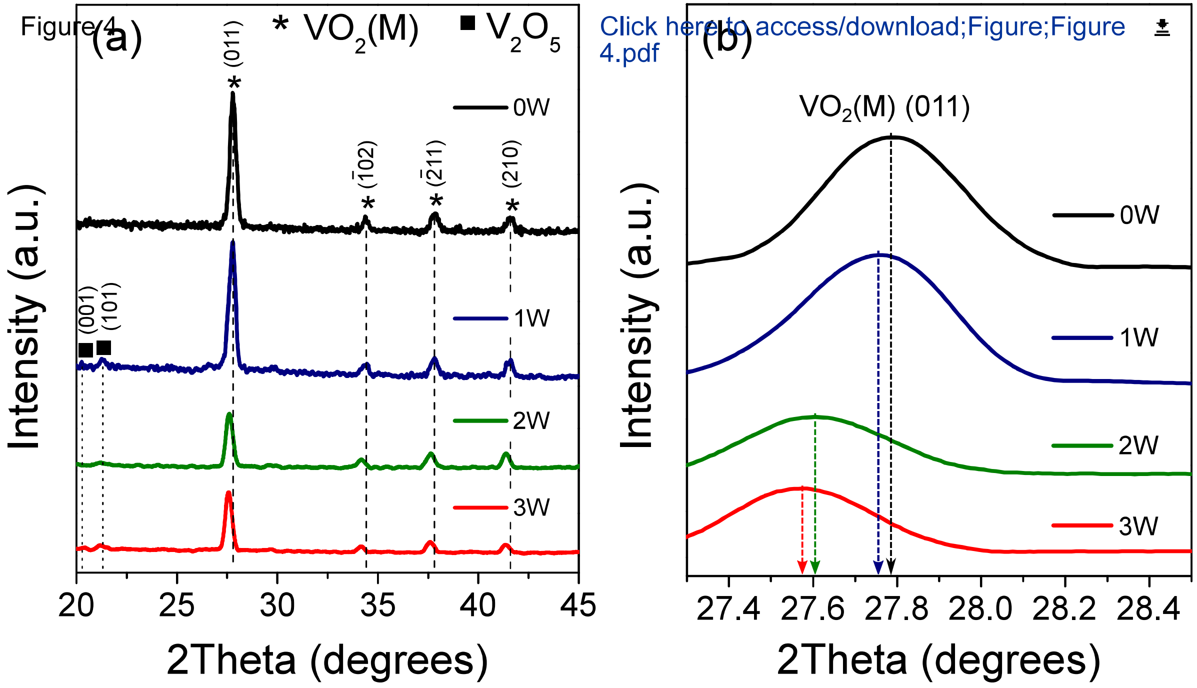
(a)
* VO$_2$(M)
■ V$_2$O$_5$
(011)
(̄102)
(̄211)
(210)
(001)
(101)
0W
1W
2W
3W
Intensity (a.u.)
20
25
30
35
40
45
2Theta (degrees)
(b)
VO$_2$(M) (011)
0W
1W
2W
3W
Intensity (a.u.)
27.4
27.6
27.8
28.0
28.2
28.4
2Theta (degrees)

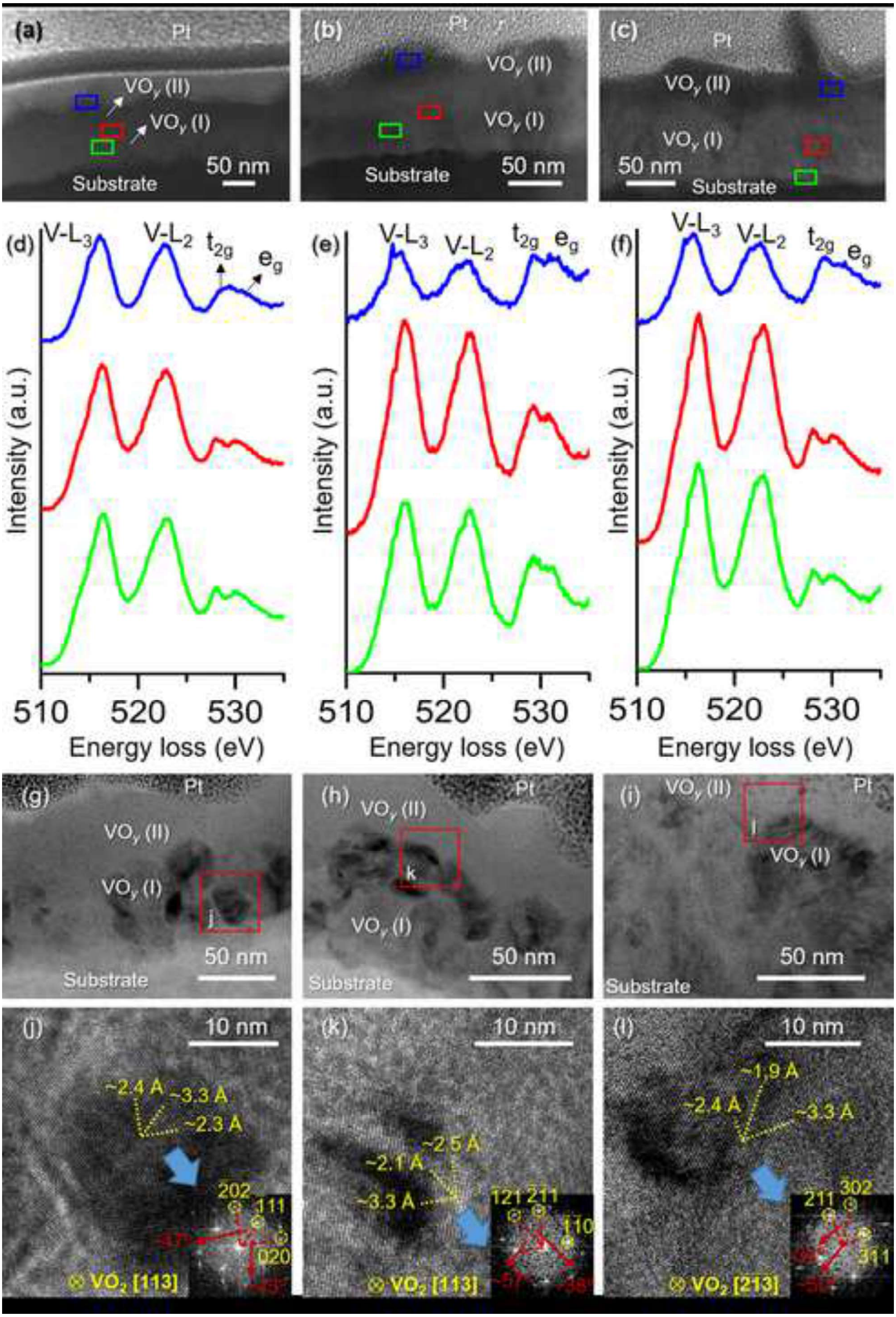
(a)
Pt
VO$_y$ (II)
VO$_y$ (I)
Substrate
50 nm
(b)
Pt
VO$_y$ (II)
VO$_y$ (I)
Substrate
50 nm
(c)
Pt
VO$_y$ (II)
VO$_y$ (I)
50 nm
Substrate
(d)
V-L$_3$
V-L$_2$
t$_{2g}$
e$_g$
Intensity (a.u.)
510
520
530
Energy loss (eV)
(e)
V-L$_3$
V-L$_2$
t$_{2g}$
e$_g$
Intensity (a.u.)
510
520
530
Energy loss (eV)
(f)
V-L$_3$
V-L$_2$
t$_{2g}$
e$_g$
Intensity (a.u.)
510
520
530
Energy loss (eV)
(g)
Pt
VO$_y$ (II)
VO$_y$ (I)
j
50 nm
Substrate
(h)
VO$_y$ (II)
Pt
k
VO$_y$ (I)
50 nm
Substrate
(i)
VO$_y$ (II)
Pt
l
VO$_y$ (I)
50 nm
Substrate
(j)
10 nm
~2.4 Å
~3.3 Å
~2.3 Å
202
111
020
⊗ VO$_2$ [113]
(k)
10 nm
~2.5 Å
~2.1 Å
~3.3 Å
121
211
110
⊗ VO$_2$ [113]
(l)
10 nm
~1.9 Å
~2.4 Å
~3.3 Å
211
302
311
⊗ VO$_2$ [213]

Figure 6

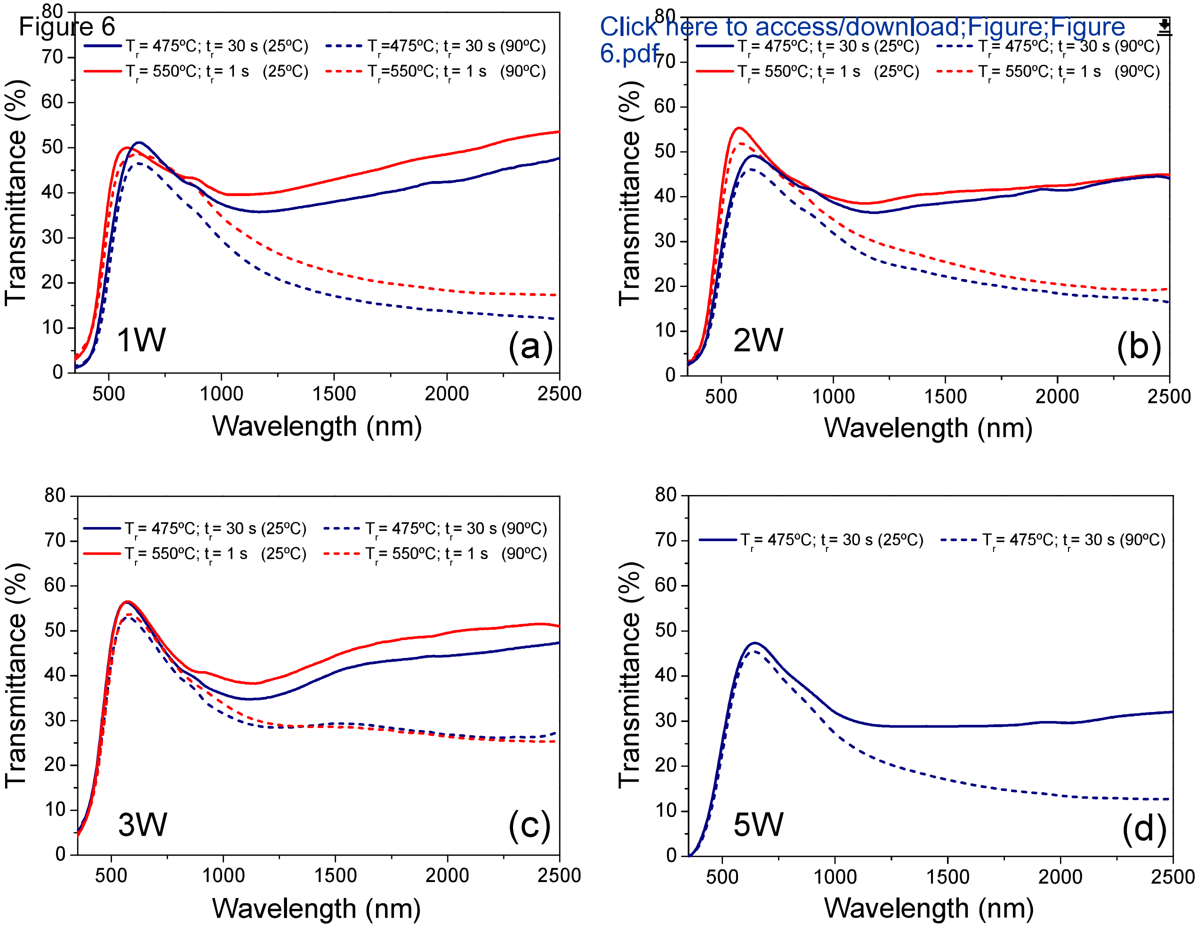
T_r= 475ºC; t_r= 30 s (25ºC)
T_r=475ºC; t_r= 30 s (90ºC)
T_r= 550ºC; t_r= 1 s (25ºC)
T_r=550ºC; t_r= 1 s (90ºC)
1W
(a)
T_r= 475ºC; t_r= 30 s (25ºC)
T_r= 475ºC; t_r= 30 s (90ºC)
T_r= 550ºC; t_r= 1 s (25ºC)
T_r= 550ºC; t_r= 1 s (90ºC)
2W
(b)
T_r= 475ºC; t_r= 30 s (25ºC)
T_r= 475ºC; t_r= 30 s (90ºC)
T_r= 550ºC; t_r= 1 s (25ºC)
T_r= 550ºC; t_r= 1 s (90ºC)
3W
(c)
T_r= 475ºC; t_r= 30 s (25ºC)
T_r= 475ºC; t_r= 30 s (90ºC)
5W
(d)
Transmittance (%)
Wavelength (nm)
0
10
20
30
40
50
60
70
80
500
1000
1500
2000
2500

Figure 7

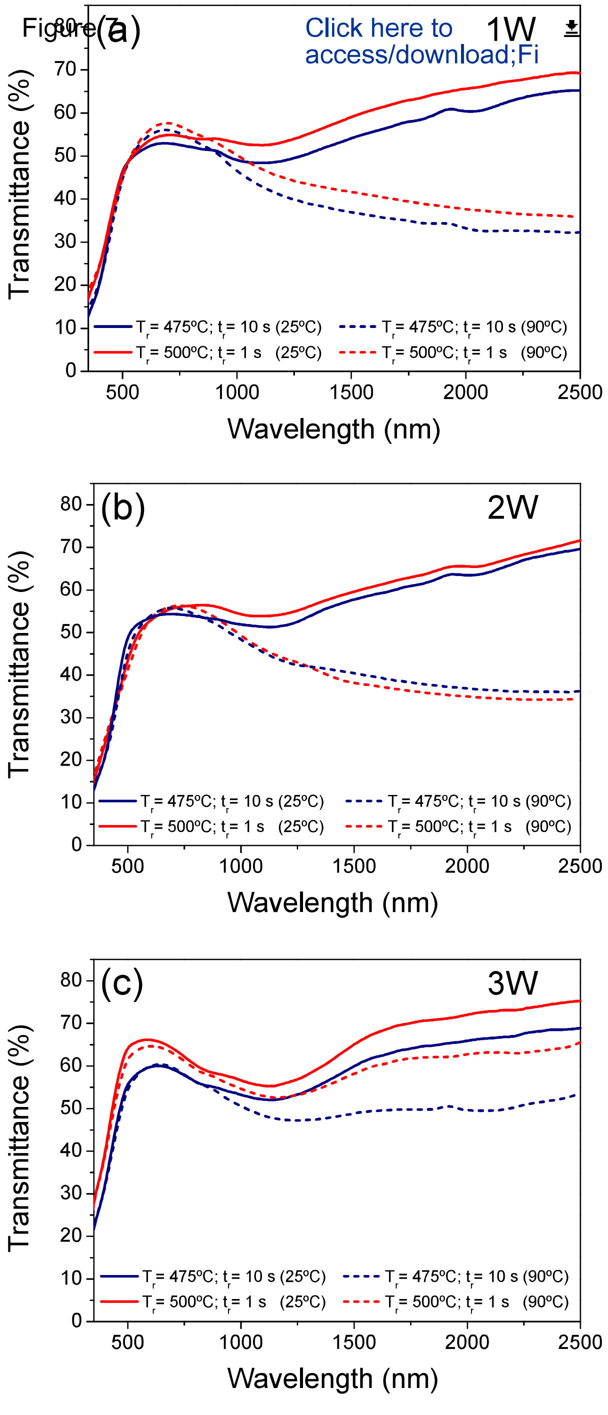
(a)
1W
Transmittance (%)
0
10
20
30
40
50
60
70
80
500
1000
1500
2000
2500
Wavelength (nm)
Tr= 475ºC; tr= 10 s (25ºC)
Tr= 500ºC; tr= 1 s (25ºC)
Tr= 475ºC; tr= 10 s (90ºC)
Tr= 500ºC; tr= 1 s (90ºC)
(b)
2W
Transmittance (%)
0
10
20
30
40
50
60
70
80
500
1000
1500
2000
2500
Wavelength (nm)
Tr= 475ºC; tr= 10 s (25ºC)
Tr= 500ºC; tr= 1 s (25ºC)
Tr= 475ºC; tr= 10 s (90ºC)
Tr= 500ºC; tr= 1 s (90ºC)
(c)
3W
Transmittance (%)
0
10
20
30
40
50
60
70
80
500
1000
1500
2000
2500
Wavelength (nm)
Tr= 475ºC; tr= 10 s (25ºC)
Tr= 500ºC; tr= 1 s (25ºC)
Tr= 475ºC; tr= 10 s (90ºC)
Tr= 500ºC; tr= 1 s (90ºC)

Figure 8

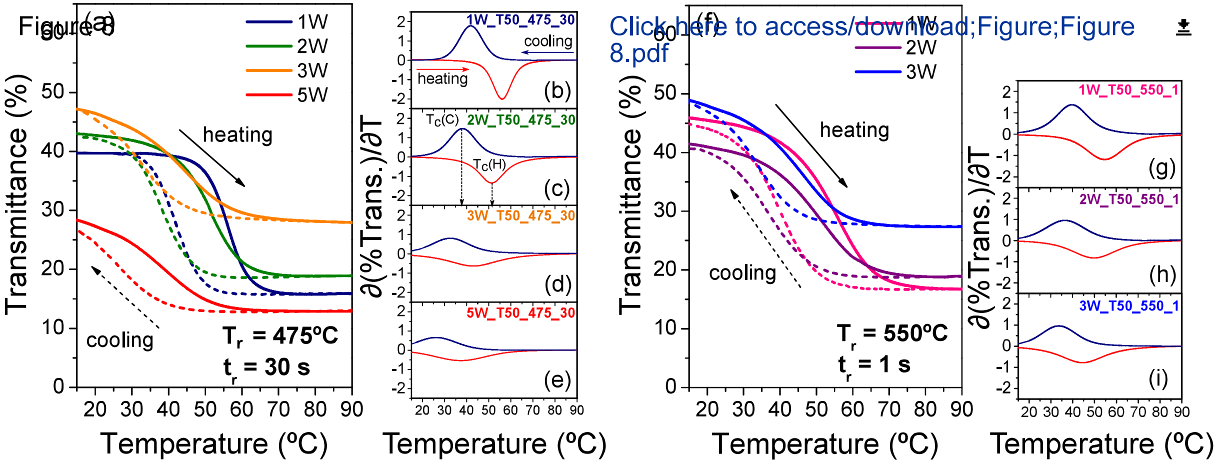
(a)
Transmittance (%)
0
10
20
30
40
50
60
20 30 40 50 60 70 80 90
Temperature (ºC)
1W
2W
3W
5W
heating
cooling
T_r = 475ºC
t_r = 30 s
∂(%Trans.)/∂T
1W_T50_475_30
cooling
heating
(b)
T_C(C)
2W_T50_475_30
T_C(H)
(c)
3W_T50_475_30
(d)
5W_T50_475_30
(e)
2
1
0
-1
-2
20 30 40 50 60 70 80 90
Temperature (ºC)
(f)
Transmittance (%)
1W
2W
3W
heating
cooling
T_r = 550ºC
t_r = 1 s
Temperature (ºC)
∂(%Trans.)/∂T
1W_T50_550_1
(g)
2W_T50_550_1
(h)
3W_T50_550_1
(i)
Temperature (ºC)

Figure 9

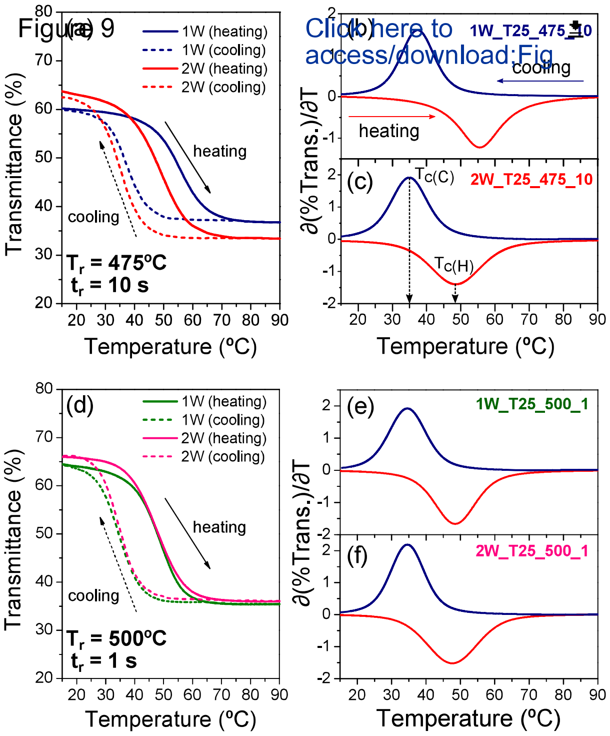
(a)
1W (heating)
1W (cooling)
2W (heating)
2W (cooling)
heating
cooling
T_r = 475ºC
t_r = 10 s
Transmittance (%)
Temperature (ºC)
(b)
1W_T25_475_10
cooling
heating
(c)
2W_T25_475_10
$T_{C(C)}$
$T_{C(H)}$
∂(%Trans.)/∂T
Temperature (ºC)
(d)
1W (heating)
1W (cooling)
2W (heating)
2W (cooling)
heating
cooling
T_r = 500ºC
t_r = 1 s
Transmittance (%)
Temperature (ºC)
(e)
1W_T25_500_1
(f)
2W_T25_500_1
∂(%Trans.)/∂T
Temperature (ºC)

Table 1. Deposition and thermal annealing conditions for the samples addressed in this study. τ_N is the nominal layer thickness, T_r is the reaction temperature, t_r is the reaction time.

Sample	**W doping (at.%) in $V_xW_{1-x}O_2$**	**τ_N (nm)**	**Number of $V_{0.85}W_{0.15}O_y$ multilayers**	**T_r (ºC)**	**t_r (s)**
1W_T50_475_30	0.33	50	8	475	30
1W_T50_550_1				550	1
1W_T25_475_10		25	4	475	10
1W_T25_500_1				500	1
2W_T50_475_30	0.67	50	12	475	30
2W_T50_550_1				550	1
2W_T25_475_10		25	6	475	10
2W_T25_500_1				500	1
3W_T50_475_30	1.00	50	12	475	30
3W_T50_550_1				550	1
3W_T37.5_525_1		37.5	9	525	1
3W_T25_475_10		25	6	475	10
3W_T25_500_1				500	1
5W_T50_475_30	1.67	50	12	475	30

Table 2. Radiometric and photometric parameters changes upon heating for all the studied samples. For a detailed definition and explanation of how all these parameters are obtained, refer to the work by Outón *et al.* (Appendix A)[52]. The accuracy of these values is ±0.1%.

Sample	**T_{lum} (%)**	**ΔT_{lum} (%)**	**ΔT_{sol} (%)**	**$\Delta T_{sol,\ rel}$ (%)**	**ΔT_{IR} (%)**	**$\Delta T_{IR,\ rel}$ (%)**
1W_T50_475_30	39.6	3.7	7.2	19.9	12.6	32.0
1W_T50_550_1	45.5	2.8	5.3	13.4	10.6	24.8
1W_T25_475_10	50.2	-0.9	2.8	5.8	7.8	14.9
1W_T25_500_1	50.9	-1.1	2.9	5.7	8.1	14.5
2W_T50_475_30	39.4	2.2	5.8	15.9	10.4	26.0
2W_T50_550_1	49.2	3.8	5.0	12.4	8.4	20.5
2W_T25_475_10	51.3	0.9	3.9	7.9	8.5	15.5
2W_T25_500_1	49.1	0.9	4.7	9.3	10.6	18.6
3W_T50_475_30	51.7	3.5	4.4	10.8	6.9	17.6
3W_T50_550_1	52.0	3.2	5.2	12.4	9.1	21.6
3W_T37.5_525_1	47.8	2.7	4.4	10.9	8.0	19.4
3W_T25_475_10	58.0	0.3	2.5	4.5	5.3	9.4
3W_T25_500_1	64.4	1.9	2.4	4.1	3.5	5.8
5W_T50_475_30	37.2	2.0	4.1	12.8	7.2	22.1

Table 3. Main features of the thermochromic hysteresis loops of all the studied samples. T_c denotes the temperatures of the MIT transition on heating; W_H is the hysteresis loop width given by the differences of the MIT temperatures on heating and cooling cycles; ΔT_{rel} is the relative decrease of transmittance upon the transition at 2000 nm; and S_H is the hysteresis smoothness. The accuracy of temperature and transmittance values are ±0.5ºC and ±0.1%, respectively.

Sample	**T_c (ºC)**	**W_H (ºC)**	**ΔT_{rel} (%)**	**S_H (ºC)**
1W_T50_475_30	56	14	59.9	12
1W_T50_550_1	55	15	63.5	20
1W_T25_475_10	56	19	39.0	14
1W_T25_500_1	48	13	45.0	14
2W_T50_475_30	51	13	56.0	16
2W_T50_550_1	50	14	54.4	23
2W_T25_475_10	48	13	47.9	16
2W_T25_500_1	48	13	45.3	15
3W_T50_475_30	43	10	40.9	24
3W_T50_550_1	44	10	44.3	22
3W_T37.5_525_1	43	10	48.3	29
5W_T50_475_30	37	11	54.6	26